Airborne Metal Toxin Particulate Signatures and Legacy at Wildland–Urban Interface

Alireza Namayandeh[1,4], Charles Lamb[1], Frida D. Garcia-Ledezma[1], Jonathon Howell[1], Catherine Erol[1], Dan Kubota[1], Raphael Kim[2], Charise Young[3], Katie Huy[1], Scott Fendorf[1,4]

[1]Department of Earth System Science, Stanford University, Stanford, CA, USA.

[2]Department of Bioengineering, School of Engineering, Stanford University, Stanford, CA, USA

[3]Department of Chemistry, Pomona College, Claremont, CA, USA

[4]King Center on Global Development, Stanford University, Stanford, CA, USA

Authors email addresses: arnama@stanford.edu, clamb8@stanford.edu, fdgarci2@stanford.edu, jh4653@stanford.edu, cerol@stanford.edu, dkubota@stanford.edu, raphaelk@stanford.edu, charisedyoung@gmail.com, khuy@stanford.edu, fendorf@stanford.edu

Corresponding author:

Alireza Namayandeh- Current address: Stanford University; 367 Panama St, Stanford, CA 94305, Fendorf@stanford.edu

Preprint statement:

This manuscript is a non-peer-reviewed preprint submitted to EarthArXiv.

Airborne Metal Toxin Particulate Signatures and Legacy at Wildland–Urban Interface

Alireza Namayandeh[1,4], Charles Lamb[1], Frida D. Garcia-Ledezma[1], Jonathon Howell[1], Catherine Erol[1], Dan Kubota[1], Raphael Kim[2], Charise Young[3], Katie Huy[1], Scott Fendorf[1,4]

Author Affiliations:

[1]Department of Earth System Science, Stanford University, Stanford, CA, USA.

[2]Department of Bioengineering, School of Engineering, Stanford University, Stanford, CA, USA

[3]Department of Chemistry, Pomona College, Claremont, CA, USA

[4]King Center on Global Development, Stanford University, Stanford, CA, USA

ABSTRACT

Wildland–urban interface (WUI) fires burn urban materials together with soil and vegetation, generating air pollution as smoke during active burning and as resuspended dust during recovery. Here, we combine size-resolved sampling of the Eaton Fire (Altadena, CA) with controlled resuspension of materials collected from properties affected by the Eaton and Palisades (Pacific Palisades, CA) fires. Lead is a clear urban-fire signature when compared with wildland-fire smoke, with ~60% of total Pb residing in the ultrafine fraction. By contrast, Cr in urban smoke remained within the wildland-fire range and followed the geologic composition of the fire perimeter. During resuspension, however, vehicle-associated debris produced >50-fold ultrafine Pb enrichment and >100-fold ultrafine Cr enrichment. Bulk source-metal concentrations alone did not predict airborne Pb and Cr release; total Cr release instead tracked the resuspendable particulate pool behavior. The metal toxins occurred as nanoparticles smaller than 10 nm and as multi-metal aggregates containing Pb, Cu, Zn, Cr, Fe, Ni, and Ti in both smoke and resuspended particulates. Our results establish WUI fires as combustion–resuspension systems in which metal signatures evolve between active burning and post-fire resuspension, providing a basis for phase-specific monitoring, cleanup controls, and exposure protection.

INTRODUCTION

Wildland–urban interface (WUI) fires are emerging as a distinct and increasingly important form of fire smoke and dust exposure.[1] These fires act as combustion–resuspension systems that transform natural and urban materials into airborne metal-bearing particles.[1, 2] Unlike wildland fires, whose emissions are dominated by biomass with soil and geological imprints,[3, 4] WUI fires burn wildland soil and vegetation together with vehicles, homes (and associated infrastructure), producing an integrated smoke plume.[5-8] Post-fire, the burned landscape remains as ash and debris that contain toxic fire-altered materials that can be re-entrained by wind, cleanup, and reconstruction.[9, 10] Thus, the integrated smoke and post-fire dust represent exposure pathways within the WUI fire system, with toxins becoming airborne at different times.[6, 7]

The January 2025 LA fires illustrate the impact of the WUI fires, where approximately 17 million Southern California residents were under a smoke advisory.[11] The Eaton and Palisades fires, ignited on January 7, 2025, burned approximately 14,021 and 23,448 acres, respectively, caused at least 31 fatalities and displaced large populations, destroyed more than 16,000 structures, and left extensive debris requiring cleanup.[6, 12-14] Wildland landscapes accounted for 33% and 38% of the combustible fuel mass within the Eaton and Palisades burn zones, respectively; structures and vehicles accounted for the remaining 67% and 62%, respectively.[8] The airborne particulates therefore likely reflected both natural and urban-material sources during active burning, followed by continuing resuspension of fire-altered materials during recovery.[6]

The mixed source landscape of WUI fires is important because each phase can contribute a different toxin metal particulate signature to the air. During wildland burning, metals are derived from vegetation and soil, producing smoke that can contain Cr, Ni, Ti, Fe, Mn, and other geologically derived elements.[3, 4] Previous wildfire-smoke measurements have shown that metal-bearing particulates can be abundant, and that their abundance can be related to the geologic composition of the fire perimeter.[3] In contrast, the

combustion of urban materials can introduce anthropogenic metals that yield new urban signatures, ranging from the historic (and present) use of Pb to the recent use of Co and Li.[5, 15-19] Post-fire, altered materials remain in the burned landscape and can continue to generate airborne particles through wind, cleanup, and reconstruction.[20, 21]

Conventional $PM_{2.5}$ measurements and bulk soil or debris metal concentrations remain essential for evaluating smoke exposure and post-fire contamination. However, they are only the start. Critically important is recognizing how toxic metals vary with fire position, their legacy post-fire, and their presence in fine to ultrafine particles that may become metal-enriched. [3, 21, 22 6, 21 23-25] Identifying these signatures is important because different phases of a WUI fire may require different monitoring strategies, exposure controls, and public-health guidance.

Here, we identify metal signatures of airborne particulates from different stages of WUI fires and their legacy in post-fire derived dust. By combining size-resolved smoke sampling with controlled resuspension of fire-altered materials, we evaluate WUI fires as combustion–resuspension systems that generate metal toxin particulates across active-fire and post-fire phases. This approach links the sources and particle-size distributions of airborne metals to their potential implications for inhalation exposure and public health.

RESULTS AND DISCUSSION

Toxic Metals in Smoke. Toxic metals were present within the smoke of the Eaton Fire from the time of its origin and illustrated a rapid increase in urban toxins. Air monitoring data from an EPA sensor (Fig. S1) showed a sharp increase in Pb concentrations immediately following the Eaton fire, reaching 440 ± 110 ng m^{-3} on Jan 8, which then declined to 41.8 ± 11 ng m^{-3} on January 10. Zinc, Cu, and Fe also showed substantial increases, while other elements, including Cr, Ti, Ni, and Mn, exhibited more moderate post-fire increases followed by progressive decreases after Jan 13. Metal concentrations of our smoke samples

from Jan 10 showed the highest total concentration (503.6 ± 111 ng m^{-3}) for Fe, followed by Cr (87.73 ± 15.6 ng m^{-3}), Ti (57.88 ± 8.01 ng m^{-3}), and Cu (50.30 ± 17.2 ng m^{-3}). Total Pb concentrations were also elevated at 18.36 ± 2.76 ng m^{-3}. (Fig. 1).

Metals were distributed across the full particle-size spectrum, with a recurring presence in the fine (<0.25 µm-2.5 µm) and ultrafine fractions (<0.25 µm) (Fig. 1). Lead was predominantly enriched in the ultrafine fraction, accounting for approximately 60% of its total measured concentration (Fig. S2). Chromium and Ni also showed substantial enrichment in the ultrafine fraction, with approximately 35% of their total concentrations associated with the ultrafine fraction. In contrast, less than 30% of Fe, Cu, Ti, Zn, and Mn were present in the ultrafine fraction, although these elements remained strongly associated with the fine particles. The strong enrichment of Pb and Cr in ultrafine particles combines the inherent toxicity of these metals with the enhanced inhalation exposure potential associated with their small aerodynamic diameter.

Air-quality index (AQI) and soil-screening benchmarks provide essential first-order information about smoke exposure and post-fire contamination, respectively.[4, 26-29] Considering airborne metal composition, particle-size distribution, and resuspension potential alongside these benchmarks can provide a more complete assessment of inhalation exposure during active burning and post-fire recovery. During Eaton Fire smoke sampling, the average $PM_{2.5}$ concentration was 36.2 µg m^{-3}. This concentration falls within the range used for the U.S. EPA's 24-h "Unhealthy for Sensitive Groups" AQI category. Nevertheless, $PM_{2.5}$ mass alone did not capture the substantial concentrations of toxic metals or provide information about their size distribution. At the time of the fire, this information was not included in the $PM_{2.5}$-based air-quality information available to the public, despite their severe health impacts.[30-34]

Metal Signatures of Eaton Fire Smoke

The presence of Pb in the smoke of the LA fires is consistent with previous observations that these metals are enriched in WUI fires due to the combustion of anthropogenic materials.[3, 5, 9, 35] We compared Pb concentrations measured in our Eaton Fire smoke samples and the highest concentration recorded by the

EPA sensor with the Pb concentration in smoke from the ten wildland fires measured in this study. Lead concentrations in wildland-fire smoke were below 10 ng m^{-3}, whereas the EPA sensor recorded values as high as 438.96 ± 109.80 ng m^{-3} immediately after the Eaton Fire started (Fig. 2). This substantial enrichment identifies Pb as a strong signature of urban-material contributions to WUI fire smoke. By contrast, Cr concentrations fell within the range observed for wildland fires (Fig. 2b).

To account for differences in smoke concentrations among fires, we normalized Pb and Cr concentrations by the average $PM_{2.5}$ concentration during each sampling period. Relative to the highest concentration measured among the wildland fires, Pb in our Eaton Fire sample was approximately 250% higher after normalization. Chromium remained within the range observed across wildland fires when normalized to average $PM_{2.5}$ concentration (Fig. 2c and d). Wildland-fire $PM_{2.5}$ is largely derived from biomass burning and surficial soils of the natural landscape,[3, 36-38] whereas $PM_{2.5}$ in WUI-fire smoke can also include materials released from the combustion of structures, vehicles, and other anthropogenic sources.[5, 8, 9, 39] Further, Pb enrichment cannot be explained by differences in biomass concentration alone as noted by Pb enrichment per unit $PM_{2.5}$. By contrast, the comparable Cr-to-$PM_{2.5}$ ratios provide no evidence of distinct Cr enrichment from urban materials during active burning and are consistent with a Cr source shared with wildland fires.

We recently showed that metal concentrations in wildfire smoke reflect the total metal content of the underlying lithology and can be fit to (or predicted by) a geological composition index (GCI).[3] Here, we show that Cr concentrations (normalized to K as biomass tracer) increased linearly with increasing GCI ($R^2 = 0.59$, $p = 0.02$; Fig. 3a), indicating that its concentration in smoke is consistent with the metal content of the underlying lithology. This relationship was even stronger for ultrafine Cr-bearing particles, for which normalized Cr concentrations increased with GCI ($R^2 = 0.89$, $p < 0.001$; Fig. 3b). The concentration of K is provided in Table S2. Using the generalized GCI to wildfire relationship, predicted total and ultrafine Cr/K ratios are 0.122 and 0.037, respectively, for the lithology of Eaton fire perimeter (Fig. S3) and compare closely with measured values for the Eaton fire (0.117 ± 0.028 for total Cr/K and 0.042 ± 0.010 for ultrafine

Cr/K) (Fig. 3). Thus, relationships derived exclusively from the wildland fires (without urban input) predicted both the total and ultrafine Cr/K ratios measured in the Eaton Fire. Text S1 explains the calculation of GCI for Eaton Fire, and Table S3 shows the information used to calculate GCI.

Metals in Resuspended Particulates

Following fire suppression, fire-altered material remaining at impacted properties can continue to generate airborne (ultra)fine metal-bearing particulates through wind-driven resuspension and clean-up (e.g., debris removal) and construction activities. To investigate this source of exposure and establish a source-to-airborne particulate relationship, we designed and fabricated a windbox that utilizes the same active air-sampling system used for smoke collection to separate, size-segregate, and characterize resuspendable particulates (Less than 10 μm in diameter). We collected and characterized seven fire-altered samples from Eaton Fire (EF)- and Palisades Fire (PF)-impacted houses (sample names and characteristics are provided in Table S1 and Fig. S4). Metals were measured across all fire-altered materials. Iron was the most abundant metal, with concentrations ranging from 5089.0 ± 901 to 15115 ± 1260 (Fig. S5). Lead was also present at high concentrations, ranging from 332.25 ± 22.1 to 14599 ± 849 μg g^{-1} across the samples. Other metals consistently observed at high concentrations included Cr, Cu, Ti, Zn, Mn, and Ni. These samples were resuspended in the windbox at speeds consistent with a gentle breeze (16 km h^{-1}). The potential for resuspension of different fire-altered materials varied substantially, ranging from 0.56 ± 0.06 mg (sample PFB) to 10.2 ± 0.7 mg (sample EFC) (Table S1). The ultrafine particulates ranged from a low of only ~3.30 % (sample PFA) to a high of ~34.8 % of the total resuspended particulates (sample EFD). On average, the generated resuspended material consisted of 45.5 ± 4.7% coarse (>2.5 μm), 39.2 ± 2.3 % fine, and 15.3 ± 4.4 % ultrafine particulates (Fig. S6).

Airborne metal concentrations also varied substantially in the resuspended particulates. The absolute concentration of total Pb ranged from 0.666 ± 0.043 μg m^{-3} for sample EFB to 51.04 ± 6.0 μg m^{-3} for sample PFB (Fig. S7). Chromium showed less variability, ranging from 0.261 ± 0.043 μg m^{-3} for sample EFB to 1.99 ± 0.17 μg m^{-3} for sample PFC. Similar sample-to-sample variability was observed for the other

169 metals such as Fe, Zn, Cu, Ni, Mn, and Ti across aerodynamic diameter fractions, with substantial
170 concentrations extending into the fine and ultrafine particles. To account for differences in the quantity of
171 resuspended particulates, we also evaluated mass-normalized metal concentrations. The distribution of
172 mass-normalized concentrations showed higher median concentrations of Cr, Pb, Cu, and Fe in the ultrafine
173 fraction than in the larger particle diameter fractions (Fig. S8). On average, Fe and Zn were the most
174 abundant metals in the resuspended particulates, each accounting for approximately 25% of the total
175 airborne metal mass. Titanium contributed approximately 17%, followed by Pb (11%), Cu (10%), Mn (6%),
176 and Cr and Ni (1% each). The remaining metals each accounted for less than 3% of the total airborne metal
177 mass (Fig. S9). These relative abundances were generally consistent across aerodynamic diameter fractions,
178 except for Cr, which showed preferential enrichment in the ultrafine fraction. In this fraction, Cr accounted
179 for approximately 4% of the total metal mass, compared with ~1% of the total resuspended mass.

180 We examined the impact of fire-altered materials on the abundance of airborne metals using both
181 parametric and non-parametric approaches. Most source–air relationships were weak and nonsignificant
182 (Figs. S10 and S11). These results indicate that the amount of metal present in the fire-altered materials
183 alone did not consistently predict the amount released into the airborne fraction. The absence of consistent
184 source–air relationships suggests that additional physical properties control post-fire airborne metal release.
185 We therefore developed an absolute-mass model incorporating the collected resuspendable PM mass and
186 the $PM_{2.5}$ decay constant, which represent the size of the resuspendable particle pool and its depletion from
187 the airborne phase, respectively (Text S2 and Fig. S12 and S13). These parameters explained 81% of the
188 variation in total collected Pb mass ($R^2 = 0.81$, $p = 0.04$) (Fig. S14a). The corresponding Cr model explained
189 87 % of the variation and was also statistically significant ($R^2 = 0.87$, $p = 0.02$) (Fig. S14b). These results
190 suggest that airborne Pb and Cr release may be related more to the mass of resuspendable particulates in
191 the source than to their bulk concentrations in fire-altered materials.

192 **Metal Enrichment in Air**

193 We calculated metal enrichment factors by comparing metal concentrations in resuspended
194 particulates with their corresponding concentrations in fire-altered materials. Metal enrichment varied

substantially among both samples and elements, with some fire-altered materials exhibiting strong enrichment for specific metals while others showed little or no enrichment (Fig. 4 and Table S4). Despite this variability, the median enrichment factors exceeded 1 for Cr, Ti, and Zn across all fractions, and for Ni in the total, fine, and ultrafine fractions but not the coarse fraction. Sample Eaton C, a melted planter ash, was the only sample enriched in all analyzed metals (Table S1 and S4). This sample also generated the greatest mass of resuspended particles (10.2 ± 0.7 mg). In contrast, vehicle-associated materials, including samples PFB, EFB, and PFC, generated lower total resuspendable particulate mass but exhibited substantially greater enrichment of metals. Sample PFB showed strong enrichment of Cr, Ti, Zn, Ni, and Pb, and sample PFC showed pronounced ultrafine Pb enrichment (>50).

Among the analyzed metals, Cr exhibited the greatest enrichment across samples, with an enrichment factor exceeding 100 in the ultrafine fraction of the sample EFB, which represents a residue from a burned ΩΩΩ. Chromium in common vehicle-associated forms, including alloys, is comparatively refractory and cannot volatilize extensively under typical WUI fire conditions.[9, 40] Instead, thermal stress, oxidation, and structural degradation during burning may fragment or embrittle Cr-bearing materials while leaving a substantial fraction of the Cr in residual materials.[41, 42] After fire suppression, geogenic Cr deposited from smoke may mix with Cr released from burned manufactured materials, forming a mixture of Cr-bearing material in ash, debris, and surface dust. This material can subsequently become airborne through wind-driven resuspension and activities such as cleanup, debris removal, and reconstruction, as reported by Kleeman et al.[6] Here, we used selected samples in resuspension experiments to evaluate the potential airborne mobility of metals. Currently, the contributions of different urban materials across the WUI system to airborne Cr during resuspension remain unclear. Further research, including resuspension experiments using a broader range of potential sources collected across a larger spatial area and combined with field data, is needed to determine the contributions of different urban sources to airborne metals and their impacts on air quality after WUI fires.

Identification of Metal Nanoparticles Across Fire Phases

To characterize the size, morphology, and elemental associations of particles in the smoke and resuspended particulates, STEM was performed on the fine and ultrafine fractions. Lead-bearing nanoparticles smaller than 100 nm, exhibiting faceted angular morphologies, were observed embedded within chain-like soot particles in the smoke (Fig. 5a). Lead was also identified in smoke as aggregated nanoparticles associated with Cu- and Zn-bearing particles (Fig. S14a). Chromium-bearing particles were observed across a broad size range, from less than 100 nm to approximately >500 nm, and exhibited irregular morphologies associated with Fe, Ni, Cu, and Ti in smoke (Fig. 5b). A substantial spherical and irregular Pb- and Cr- bearing nanoparticle smaller than 100 nm was also identified in resuspendable particulates (Figs. 5c, 5d, and S14b). Iron-, Ti-, and Ni-bearing nanoparticles smaller than 50 nm were also frequently identified within different particle aggregates. Individual particles frequently contained multiple metals, indicating the presence of complex multi-metal particles within wildfire smoke and resuspendable particulates, leading to a stronger toxicity response compared to exposure to a single metal.[3, 43-45] These particles exhibited a wide-range of morphologies, including spherical and rounded particles, faceted particles with sharp edges, and irregular particles, suggesting the contribution of variable pathways for their formation. Spherical nanoparticles are consistent with gas-to-particle formation pathways involving high-temperature volatilization followed by nucleation, condensation, and coagulation by cooling,[46, 47] whereas faceted and irregular particles more likely reflect entrained ash, mineral debris, or structural/vehicle-derived materials.[9, 48, 49] However, the overlap in particle characteristics in both smoke and resuspended particulates prevents clear source attribution from STEM–EDS alone, reflecting the complexity of particle formation across the active-fire and post-fire phases of WUI fires.

Our results highlight the value of considering size-dependent metal composition alongside $PM_{2.5}$ mass and bulk soil metal concentrations during active burning and post-fire resuspension. Our size-resolved measurements and STEM analyses showed that airborne particulates included metal-bearing nanoparticles as small as less than 10 nm, indicating that toxic metals are transported in particle forms capable of remaining suspended for extended periods[50, 51] and penetrating deeply into the respiratory system.[52-56]

Because toxic metals were associated with particles spanning coarse, fine, ultrafine, and nanoparticle size ranges, they have the potential to deposit throughout the respiratory tract, from the upper airways to the deep alveolar regions of the lung.[57, 58] The combination of ultrafine to nanoscale particle size and the inherent toxicity of metals such as Pb and Cr may further increase their bioavailability and potential to cross the air–blood barrier, enter the bloodstream, and reach extrapulmonary organs; inhaled ultrafine particles may also access the brain through olfactory translocation pathways.[30-34] Post-fire exposure assessments and public-health guidance can therefore build on $PM_{2.5}$ monitoring and soil-screening benchmarks by incorporating size-resolved metal composition, enrichment, and source-specific resuspension measurements. These complementary measurements are particularly relevant during cleanup and reconstruction following WUI fires, when disturbance of fire-altered materials may create continuing exposure for residents, workers, and rebuilding communities.

Materials and Methods

Smoke Collection. Smoke was sampled directly from the Eaton Fire plume on January 10 between 10:30 and 14:30. The sampling site was located approximately 10 km south of the fire center. Satellite-based smoke plume data from NOAA's Hazard Mapping System (HMS) were used to verify that the site was within the plume during the sampling period (Fig. S16). Airborne particles were collected using a Flite 4 Area Sample Pump (SKC) coupled with a Sioutas Cascade Impactor (SKC), which segregates particles into aerodynamic diameter fractions of >2.5 μm, 2.5–1.0 μm, 1.0–0.50 μm, 0.50–0.25 μm, and <0.25 μm.[3] The size-separation efficiency of the impactors has been previously characterized and is approximately 90% within the target ranges.[59] Real-time $PM_{2.5}$ concentrations were measured using an EPAM-5000 Environmental Particulate Air Monitor (SKC) equipped with a 2.5-μm impactor. Daily element concentrations from a nearby U.S. EPA Chemical Speciation Network monitor were also obtained through the Federal Land Manager Environmental Database[60] for January 4-25, 2025 (Fig. S16).

Size-resolved smoke samples were also obtained from 10 active wildfires in California, Oregon,

and Idaho between June and September 2024. Detailed fire characteristics, sampling information, and smoke maps, sampling and EPA sensor locations are provided for the wildland fires in Namayandeh et al.[3]

Fire-altered Material Collection. The fire-altered material samples were collected from four Eaton Fire-impacted houses and three Palisades Fire-impacted houses. All selected structures were completely destroyed, leaving a mixture of burned and unburned materials exposed to air for several months. This prolonged exposure increases the likelihood that these materials undergo wind-driven resuspension, making them representative sources of airborne particles following the fires. The samples were collected from burned materials with potentially high metal concentrations, including washing machines and vehicles. The general characteristics of the samples and field photographs are provided in Table S1 and Figure S4, respectively.

Resuspension Experiments. The resuspension experiments were conducted using a custom-built windbox system designed to simulate mechanical disturbance and wind-driven particle entrainment under controlled conditions. The windbox consisted of an enclosed acrylic chamber (30.5 × 25.4 × 20.3 cm; ~15.7 L internal volume), equipped with multiple airflow sources to generate turbulent and multidirectional flow, allowing for reproducible resuspension of particulates from solid substrates. Airflow within the chamber was produced using four calibrated blowers (GDSTIME 75 x 30mm**)** positioned at the corners and TriPole Mini Handheld Fan mounted along the chamber walls to promote mixing and minimize spatial heterogeneity. The blowers were calibrated to the desired wind speed using a handheld digital anemometer (AcuRite 00256M) before each experiment. This configuration creates a well-mixed environment that facilitates consistent particle suspension while avoiding strong directional bias. The chamber was used as a closed system, but no attempt was made to make it fully airtight. As a result, small, non-visible gaps inherent to the box construction allowed limited air exchange, preventing vacuum formation while remaining sufficiently closed to avoid particle loss from the chamber. Pressure differences between the interior and exterior were monitored using a manometer (ARN05M**)** and remained zero throughout the experiments. All experiments were conducted under a fume hood to ensure that incoming air was free of background particulate contamination. The schematic of the box is shown in Figure S17. For each experiment, 15 g of

material was evenly distributed across a designated area at the center of the chamber to obtain a thin layer of the samples. Airborne particle collection was achieved using the same pump and cascade impactor used for the smoke collection, as described above. Three sets of impactors were used for each experiment. In parallel, real-time $PM_{2.5}$ concentrations were continuously monitored within the chamber using an indoor air quality monitor (Hamos) to track the temporal evolution of the particle suspension during each experiment. Resuspension was initiated by activating the blowers, fans, $PM_{2.5}$ monitor, and pumps, which entrain particles into the air, maintain them in suspension, and collect them on the filters. A wind speed of 16 km h^{-1} was used to represent a gentle breeze (13–19 km h^{-1}), which commonly occurs under ambient conditions. Each experiment consisted of repeated resuspension cycles (n = 5) using the same sample, with airflow applied until $PM_{2.5}$ concentrations decayed to near-background levels (35 μg m^{-3}), at which point the cycle was terminated. After each cycle, the remaining material was swept back to the center of the chamber, and the resuspension process was repeated. Following completion of the five cycles, the remaining sample was removed, and the same fresh material was introduced. The experiment was then repeated using a new set of impactors to obtain 6 replicates in total per sample for subsequent analyses. After each experiment, the chamber was fully rinsed with soap and cleaned for the next sample.

Chemical Analysis. The resuspendable particulates and their source materials were digested using a microwave-assisted acid digestion with a mixture of nitric acid (HNO_3, 67–70%) and hydrochloric acid (HCl, 36–38%). Smoke samples collected on filters from Eaton Fire and the wildland fires were digested using the same procedure with the addition of hydrofluoric acid (HF, 49%) to ensure complete dissolution of particulate materials and accurate quantification of total elemental concentrations. This additional step was applied to the smoke samples to fully capture their ambient field composition. Measurements were performed in triplicate for most fires, except the Diamond Complex and Coffee Pot fires, for which duplicate samples were measured. Duplicate Pb measurements were reported for the Middle Fork Complex Fire.

Electron Microscopy. The morphology, size, and elemental distribution of metal-bearing particles were characterized using scanning transmission electron microscopy (STEM). TEM grids (Ted Pella) were

prepared by gently rubbing the grid surface against the particle-loaded filter to transfer collected material directly onto the grid. The grids were then lightly tapped to remove loosely attached particles before imaging. Imaging was performed in high-angle annular dark-field (HAADF) mode using a Thermo Fisher Spectra 300 monochromated, double-aberration-corrected STEM. Elemental distributions were obtained via energy-dispersive X-ray spectroscopy (EDS) using Super-X detectors. Image brightness and contrast were adjusted linearly across each micrograph to minimize the signal-to-noise ratio of the mapped pixels.

Main Figures

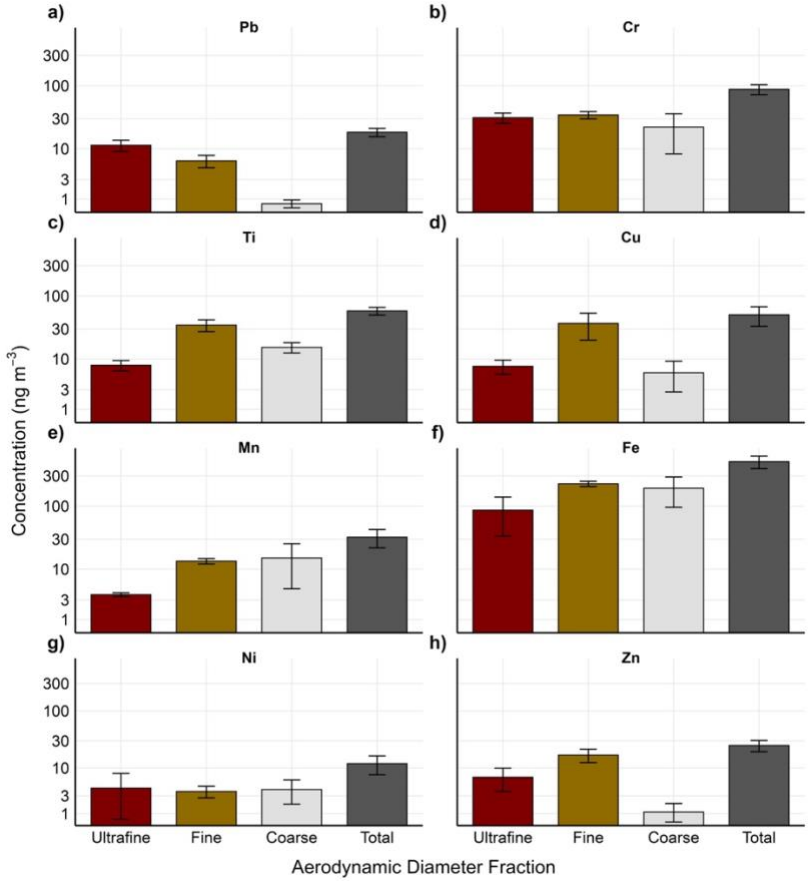

Figure 1. Concentrations of metals in Eaton fire smoke (collected on Jan 10, 2025) across particle-size fractions. Bars represent concentrations measured in ultrafine (<0.25 μm), fine (0.25–2.5 μm), coarse (>2.5 μm), and total PM samples. Error bars represent standard errors (n=3)

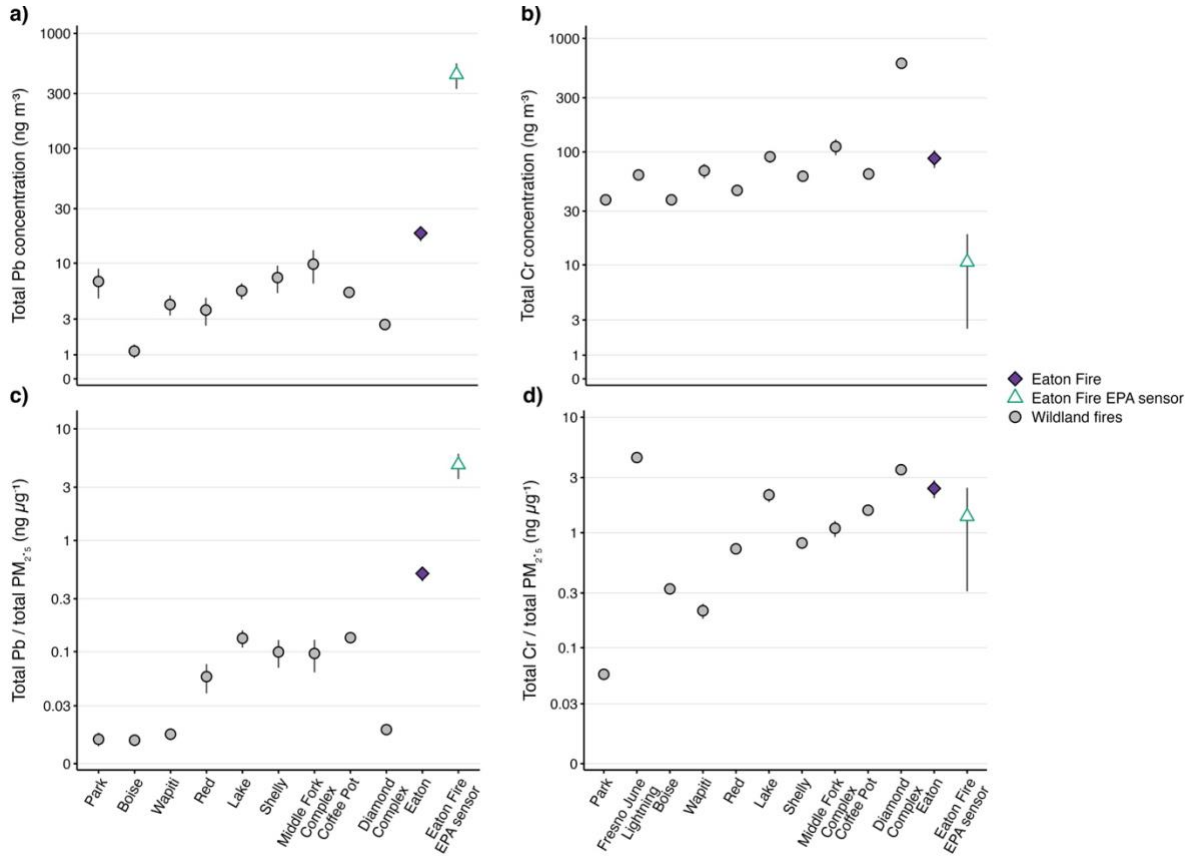

354

355 **Figure 2**. Total Pb and Cr concentrations in fire smoke samples before and after normalization to $PM_{2.5}$
356 concentration. a) total Pb and b) Cr concentrations in representative wildland-fire smoke, Eaton Fire smoke,
357 and the maximum EPA sensor measurement during the Eaton Fire period. c) Pb and d) Cr concentrations
358 normalized to total $PM_{2.5}$ for wildland-fire and Eaton Fire smoke samples. The reconstructed fine mass was
359 used for normalizing the EPA sensor sample. Lead was not reported for Fresno June Lightning Complex
360 Fire.

361

362

363

364

365

366

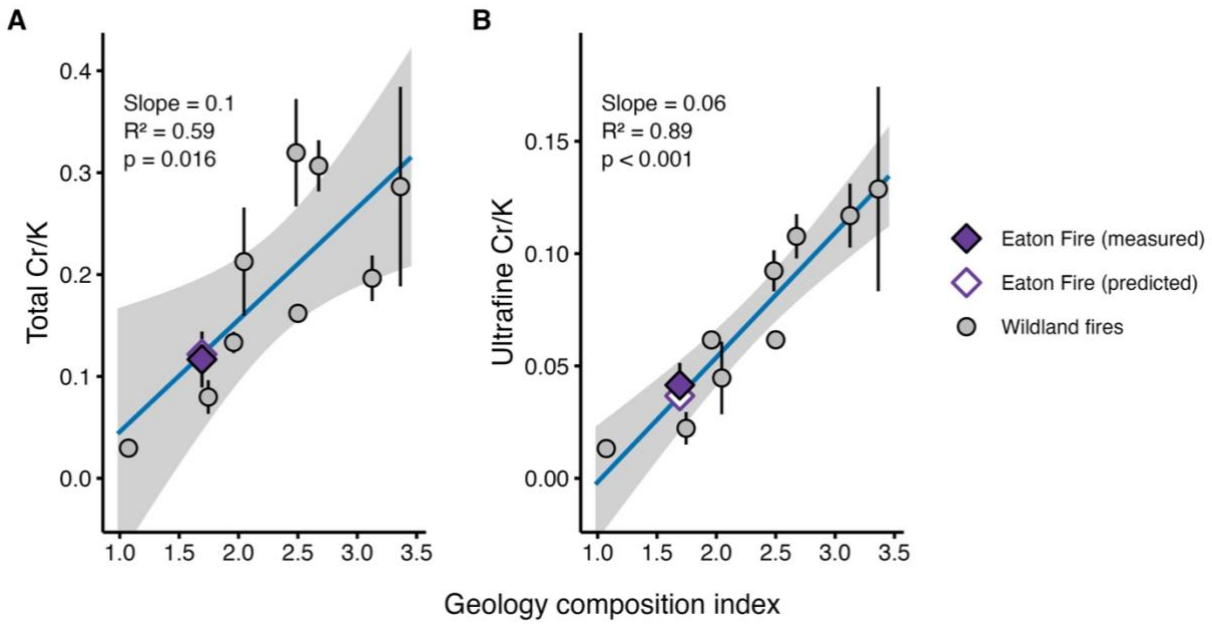

367

368 **Figure 3.** Relationships between geology composition index (GCI) and K-normalized Cr in wildland- and
369 WUI-fire smoke. (A) Total Cr/K and (B) ultrafine Cr/K (<0.25 μm aerodynamic diameter) as functions of
370 GCI. Blue lines show linear regressions fitted to nine wildland fires; the Eaton and Diamond Complex fires
371 were excluded from the fits. Diamond Complex Fire was excluded from the wildland-fire regressions
372 because it was highly influential based on Cook's distance. Its Cook's D was 3.35 for total Cr/K and 3.42
373 for ultrafine Cr/K, both substantially exceeding the conventional threshold of 4/n = 0.40 (n = 10). Gray
374 bands represent 95% confidence intervals, and error bars show propagated standard errors for the Cr/K
375 ratios. Predicted Eaton Fire was calculated by substituting the Eaton GCI into the corresponding wildland-
376 fire regression equations.

377

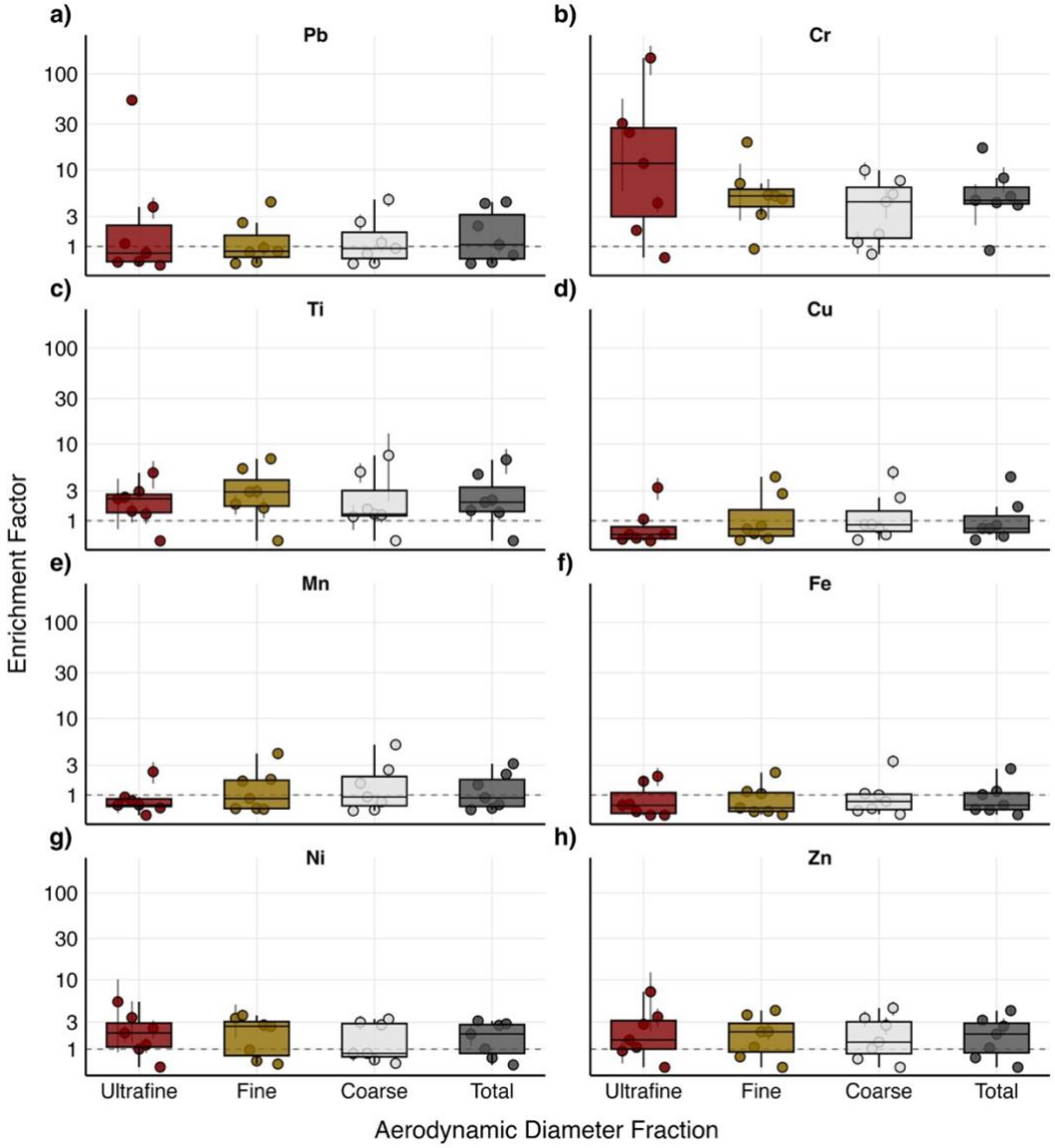

Figure 4. Metal enrichment factors in resuspended dust generated from fire-altered materials across aerodynamic diameter fractions. Enrichment factors were calculated by dividing the mass-normalized metal concentration in resuspended particulates by the corresponding metal concentration in the fire-altered material. The dashed horizontal line indicates an enrichment factor of 1, where values above 1 indicate preferential enrichment in the airborne fraction.

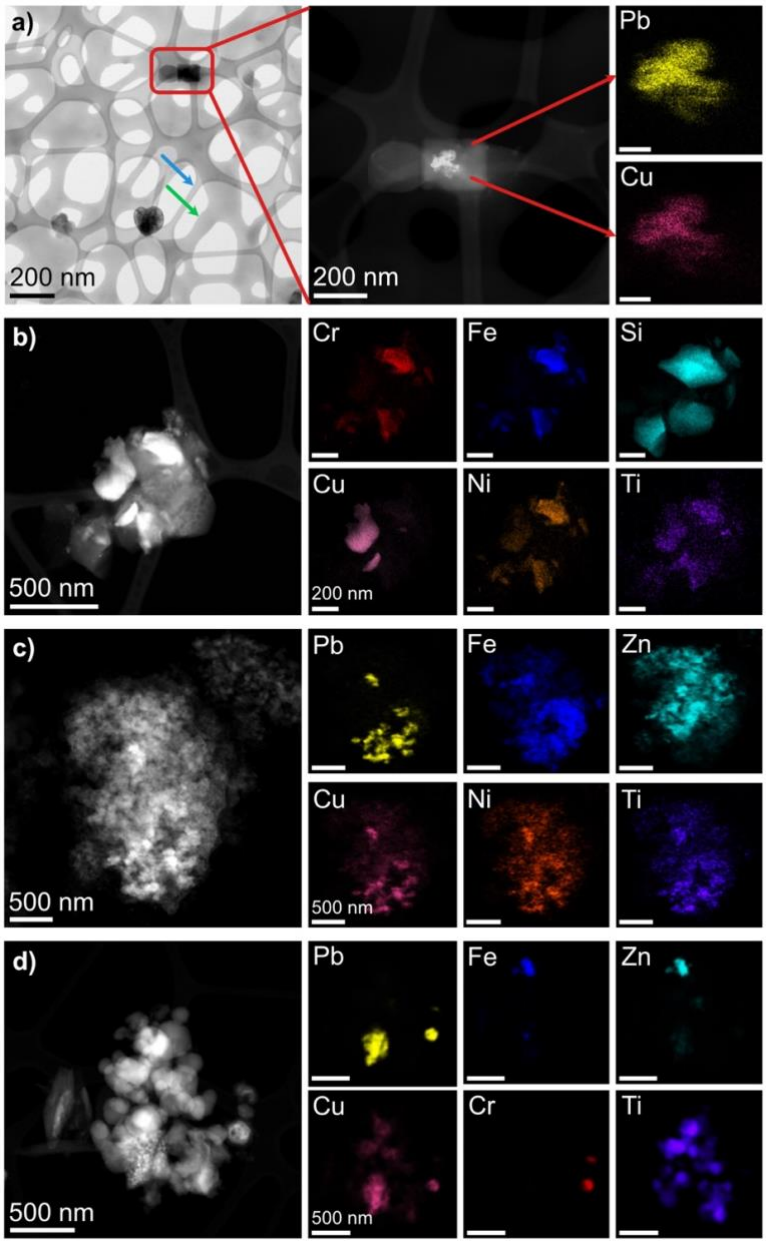

386

387 **Figure 5.** Scanning transmission electron microscopy (STEM) images and corresponding elemental maps.
388 a) Pb- and Cu-bearing nanoparticles embedded within chain-like soot particles (green arrow). The blue
389 arrow indicates the TEM grid. b**)** Cr-bearing particles in the smoke, ranging in size from <10 nm to >500
390 nm, are associated with Fe, Cu, Ni, and Ti. Si-bearing particles are also observed, with sizes exceeding 500
391 nm. c) Irregular multi-metal particles containing Pb, Cu, Fe, Ni, Zn, and Ti in resuspendable particulates
392 from sample EFA. d) Spherical and irregular Pb-bearing nanoparticle aggregates associated with Cu, Ti,
393 Zn, Fe, and Cr in resuspendable dust from sample EFC.

References

1 Schug, F. *et al.* The global wildland-urban interface. Nature 621, 94-99 (2023).

2 Jech, S. *et al.* Determination of Soil Contamination at the Wildland-Urban Interface after the 2021 Marshall Fire in Colorado, USA. Environ. Sci. Technol. 58, 4326-4333 (2024).

3 Namayandeh, A. *et al.* Toxic ultrafine to nanoparticulate materials in wildfire smoke. Preprint at https://doi.org/10.31223/X52V2D (2026).

4 Krasovich Southworth, E. *et al.* The Influence of Wildfire Smoke on Ambient PM(2.5) Chemical Species Concentrations in the Contiguous US. Environ Sci Technol 59, 2961-2973 (2025).

5 Holder, A. L., Ahmed, A., Vukovich, J. M. & Rao, V. Hazardous air pollutant emissions estimates from wildfires in the wildland urban interface. PNAS Nexus 2, pgad186 (2023).

6 Kleeman, M. J. *et al.* Airborne hexavalent chromium nanoparticles detected around cleanup zones for the 2025 Los Angeles wildfires. Commun. Earth Environ. 7, 608 (2026).

7 Baliaka, H. D. *et al.* Notes from the Field: Elevated Atmospheric Lead Levels During the Los Angeles Urban Fires - California, January 2025. Morb. Mortal. Weekly Rep. 74, 69-71 (2025).

8 Schissel, C. *et al.* Fine Spatial and Temporal Scale Fuel and Emissions Inventories for the Eaton and Palisades Wildland Urban Interface (WUI) Fires. ACS EST Air 3, 156-164 (2026).

9 Alshehri, T. *et al.* Wildland-urban interface fire ashes as a major source of incidental nanomaterials. J. Hazard. Mater. 443, 130311 (2023).

10 Baalousha, M. *et al.* Discovery and potential ramifications of reduced iron-bearing nanoparticles—magnetite, wüstite, and zero-valent iron—in wildland–urban interface fire ashes. Environ. Sci. Nano 9, 4136–4149 (2022).

11 Associated Press. Monstrous wildfires blanket Southern California with smoky air, threatening the health of millions. AP News (2025).

12 California Department of Forestry and Fire Protection. Eaton Fire. CAL FIRE Incident Archive (2025).

13 California Department of Forestry and Fire Protection. Palisades Fire. CAL FIRE Incident Archive (2025).

14 Cornwall, W. In the ashes. Science. 387, 1343-1346 (2025).

15 Boaggio, K. *et al.* Beyond Particulate Matter Mass: Heightened Levels of Lead and Other Pollutants Associated with Destructive Fire Events in California. Environ. Sci. Technol. 56, 14272-14283 (2022).

16 Alam, M. *et al.* Identification and quantification of Cr, Cu, and As incidental nanomaterials derived from CCA-treated wood in wildland-urban interface fire ashes. J. Hazard. Mater. 445, 130608 (2023).

17 Villarruel, C. M., Figueroa, L. A. & Ranville, J. F. Quantification of Bioaccessible and Environmentally Relevant Trace Metals in Structure Ash from a Wildland–Urban Interface Fire. Environ. Sci. Technol. 58, 2502-2513 (2024).

18 Kim, Y. H. *et al.* Chemical components of electric vehicle and internal combustion engine vehicle fire smoke and their mutagenic effects. Environ. Sci. Pollut. Res. 32, 26629-26639 (2025).

19 Rumi, M. J. U. *et al.* Wildland–urban interface co-combustion of biomass, synthetic polymeric materials, and lithium-ion batteries generates a new class of ultrafine soot–metal–PAH hybrid particles. Front. Public Health 14, 1768652 (2026).

20 Wagenbrenner, N. S., Chung, S. H. & Lamb, B. K. A large source of dust missing in particulate matter emission inventories? Wind erosion of post-fire landscapes. Elementa Sci. Anthropocene 5, 2 (2017).

21 Chen, H. *et al.* Characterizing Postfire Fine and Ultrafine Particles in the 2025 Eaton Fire Burn Zone and Nearby Areas. Environ. Sci. Technol. Lett. 13, 728-736 (2026).

22 Nazarenko, Y., Pal, D., Dwivedi, S. & Ariya, P. A. Air quality standards and WHO's guidance on particulate matter measuring 2.5 μm (PM2.5). Bull World Health Organ 103, 71-72 (2025).

23 Gao, Q. *et al.* High enrichment of heavy metals in fine particulate matter through dust aerosol generation. Atmos. Chem. Phys. 23, 13049-13060 (2023).
24 Rasmussen, P. E., Levesque, C., Chénier, M. & Gardner, H. D. Contribution of metals in resuspended dust to indoor and personal inhalation exposures: Relationships between PM10 and settled dust. Build. Environ. 143, 513-522 (2018).
25 Silberstein, J. M. *et al.* Residual impacts of a wildland urban interface fire on urban particulate matter and dust: a study from the Marshall Fire. Air Qual. Atmos. Health 16, 1839-1850 (2023).
26 U.S. Environmental Protection Agency. Residential Soil Lead Directive for CERCLA Sites and RCRA Hazardous Waste Cleanup Facilities. Superfund (2025).
27 California Department of Toxic Substances Control. What are acceptable concentrations of lead in soil in California? DTSC Frequently Asked Questions (2025).
28 Qiu, M. *et al.* Evaluating Chemical Transport and Machine Learning Models for Wildfire Smoke PM2.5: Implications for Assessment of Health Impacts. Environ. Sci. Technol. 58, 22880-22893 (2024).
29 K, P. & Kumar, P. A critical evaluation of air quality index models (1960–2021). Environ. Monit. Assess. 194, 324 (2022).
30 Geiser, M. & Kreyling, W. G. Deposition and biokinetics of inhaled nanoparticles. Part. Fibre Toxicol. 7, 2 (2010).
31 Nemmar, A. *et al.* Passage of inhaled particles into the blood circulation in humans. Circulation 105, 411-414 (2002).
32 Oberdorster, G. *et al.* Translocation of inhaled ultrafine particles to the brain. Inhal. Toxicol. 16, 437-445 (2004).
33 Dumkova, J. *et al.* Sub-chronic inhalation of lead oxide nanoparticles revealed their broad distribution and tissue-specific subcellular localization in target organs. Part. Fibre Toxicol. 14, 55 (2017).
34 Sanders, T., Liu, Y., Buchner, V. & Tchounwou, P. B. Neurotoxic effects and biomarkers of lead exposure: A review. Rev. Environ. Health 24, 15-45 (2009).
35 Sparks, T. L. & Wagner, J. Composition of particulate matter during a wildfire smoke episode in an urban area. Aerosol Sci. Technol. 55, 734-747 (2021).
36 Reid, J. S., Koppmann, R., Eck, T. F. & Eleuterio, D. P. A review of biomass burning emissions part II: intensive physical properties of biomass burning particles. Atmos. Chem. Phys. 5, 799-825 (2005).
37 Reid, J. S. & Hobbs, P. V. Physical and optical properties of young smoke from individual biomass fires in Brazil. J. Geophys. Res. Atmos. 103, 32013-32030 (1998).
38 Eck, T. F. *et al.* High aerosol optical depth biomass burning events: A comparison of optical properties for different source regions. Geophys. Res. Lett. 30, 2035 (2003).
39 Bowden, M., Rosario-Ortiz, F. & Mansfeldt, C. Combustion Byproducts of Individual Materials Characteristic of the Wildland-Urban Interface (WUI) Display Unique Chemical and Toxicological Profiles That Are Masked in Aggregate Samples. Environ. Sci. Technol. 59, 17198-17209 (2025).
40 Linak, W. P. & Wendt, J. O. L. Partitioning of the refractory metals, nickel and chromium, in combustion systems. Combust. Sci. Technol. 134, 291-314 (1998).
41 Lekakh, S. N., Neroslavsky, O., Li, M. & Godlevski, L. Stochastic Model for High Temperature Oxidation of Cr–Ni Austenitic Steels Assisted by Spallation. Oxid. Met. 98, 239-254 (2022).
42 Lekakh, S. N., Neroslavsky, O., Li, M., Godlewski, L. & Zhu, W. Effect of Spallation on Oxidation Kinetics of Heat-Resistant Cr–Ni Austenitic Steels on Air and Combustion Atmosphere. High Temp. Corros. Mater. 99, 79-99 (2023).
43 Yuan, Y. *et al.* In vitro toxicity evaluation of heavy metals in urban air particulate matter on human lung epithelial cells. Sci. Total Environ. 678, 301-308 (2019).

44 Sun, S. *et al.* Inhalation Bioaccessibility and Risk Assessment of Metals in PM2.5 Based on a Multiple-Path Particle Dosimetry Model in the Smelting District of Northeast China. Int. J. Environ. Res. Public Health 19, 8915 (2022).
45 Choi, Y., Park, K., Kim, I. & Kim, S. D. Combined toxic effect of airborne heavy metals on human lung cell line A549. Environ Geochem Health 40, 271-282 (2018).
46 Li, J., Pósfai, M., Hobbs, P. V. & Buseck, P. R. Individual aerosol particles from biomass burning in southern Africa: 2. Compositions and aging of inorganic particles. J. Geophys. Res. Atmos. 108, 8484 (2003).
47 Pósfai, M. *et al.* Atmospheric tar balls: Particles from biomass and biofuel burning. J. Geophys. Res. Atmos. 109 (2004).
48 Wagner, R., Jähn, M. & Schepanski, K. Wildfires as a source of airborne mineral dust: Revisiting a conceptual model using large-eddy simulation (LES). Atmos. Chem. Phys. 18, 11863-11884 (2018).
49 Benedict, K. B. *et al.* Wildland Urban Interface (WUI) Emissions: Laboratory Measurement of Aerosol and Trace Gas from Combustion of Manufactured Building Materials. ACS EST Air 1, 1673-1686 (2024).
50 Slezakova, K., Morais, S. & Pereira, M. d. C. Atmospheric nanoparticles and their impacts on public health. in Current Topics in Public Health (ed. Rodriguez-Morales, A. J.), 503–529 (IntechOpen, Rijeka, Croatia, 2013).
51 Sonwani, S. *et al.* Inhalation Exposure to Atmospheric Nanoparticles and Its Associated Impacts on Human Health: A Review. Front. Sustain. Cities 3, 690444 (2021).
52 Zhu, Q., Deng, Y.-L., Liu, Y. & Steenland, K. Associations between ultrafine particles and incident dementia in older adults. Environ. Sci. Technol. 59, 5443–5451 (2025).
53 Hu, J. *et al.* Association between exposure to ambient particulate matter and aggression among adolescents: a national school-based study in China. BMC Public Health 26, 50 (2025).
54 McDaniel, D. K. *et al.* Pulmonary exposure to Magnéli phase titanium suboxides results in significant macrophage abnormalities and decreased lung function. Front. Immunol. 10, 2714 (2019).
55 Jonasson, S., Gustafsson, Å., Koch, B. & Bucht, A. Inhalation exposure of nano-scaled titanium dioxide (TiO2) particles alters the inflammatory responses in asthmatic mice. Inhal. Toxicol. 25, 179-191 (2013).
56 Grassian, V. H., O'Shaughnessy P, T., Adamcakova-Dodd, A., Pettibone, J. M. & Thorne, P. S. Inhalation exposure study of titanium dioxide nanoparticles with a primary particle size of 2 to 5 nm. Environ. Health Perspect. 115, 397-402 (2007).
57 Darquenne, C. Aerosol deposition in health and disease. J. Aerosol Med. Pulm. Drug Deliv. 25, 140-147 (2012).
58 Rissler, J. *et al.* Deposition efficiency of inhaled particles (15-5000 nm) related to breathing pattern and lung function: an experimental study in healthy children and adults. Part. Fibre Toxicol. 14, 10 (2017).
59 Sioutas, C. *Development of new generation personal monitors for fine particulate matter (PM) and its metal content*. (Mickey Leland National Urban Air Toxics Research Center, 2004).
60 Malm, W. C., Sisler, J. F., Huffman, D., Eldred, R. A. & Cahill, T. A. Spatial and seasonal trends in particle concentration and optical extinction in the United States. J. Geophys. Res. Atmos. 99, 1347-1370 (1994).

Supplementary Information

Text S1. Geological Composition Index

Each lithological unit of Eaton Fire was assigned a relative metal-content score reflecting the typical abundance of transition metals in major rock types. Scores increased from felsic to ultramafic compositions, consistent with the general enrichment of transition metals across this lithologic sequence. Felsic units, including granite and rhyolite, were assigned a score of 1; felsic-to-intermediate units, including granodiorite and dacite, received a score of 2.5; intermediate units, including andesite and diorite, received a score of 4; intermediate-to-mafic units received a score of 4.5; mafic units, including basalt and gabbro, received a score of 5; and ultramafic units, including serpentinite, received a score of 5.5. Sedimentary and metasedimentary units with relatively low metal contents, such as sandstone, were assigned a baseline score of 1. Metamorphic rocks were scored according to their protolith, with units derived from low-metal and mafic compositions assigned scores of 1 and 5, respectively. These assignments follow established geochemical trends in which Fe, Cr, Ni, Ti, Mn, and other transition metals generally increase from felsic to ultramafic rocks.[61-64]

Mapped-unit descriptions were classified using the previously established rule-based approach.[3] Lithologic descriptions were parsed to identify diagnostic mineralogical and compositional terms, including granite, rhyolite, granodiorite, andesite, basalt, serpentinite, and peridotite, as well as compositional ranges and mixed lithologies. Where descriptions contained multiple lithologies, dominance terms such as "mostly," "primarily," and "dominantly" were used to assign the unit according to its dominant rock type.

The GCI was calculated as the area-weighted mean lithologic score within the fire perimeter:

$$GCI = \sum_i f_i \times S_i$$

where (S_i) is the assigned lithologic score for geological unit (i), and (f_i) is the fractional area of that unit within the fire perimeter. The resulting GCI represents the overall metal-enrichment potential of the geological materials within the Eaton Fire perimeter.

Text S2. Airborne Pb and Cr emission model.

To evaluate the airborne Pb and Cr release from particulate resuspension, we developed an absolute-mass model for total Pb and total Cr. For each windbox experiment, total airborne metal concentrations were calculated by summing the measured Pb or Cr concentrations across the five cascade-impactor size fractions. Real-time $PM_{2.5}$ measurements showed an initial rapid decline followed by a slower depletion phase. We therefore used a segmented regression of $\ln(PM_{2.5})$ against time to identify the breakpoint between these phases. The breakpoint was selected by minimizing the adjusted Bayesian information criterion. The slow-phase $PM_{2.5}$ decay constant, K_{slow}, was calculated as the negative slope of the regression fitted from the breakpoint through the remainder of the sampling period (Fig. S13). $PM_{2.5}$ values near background or at the instrument saturation limit were excluded, and only values between 35 and 999 $\mu g\ m^{-3}$ were used. Thus, K_{slow} represents the sustained depletion of $PM_{2.5}$ from the airborne phase following the initial rapid decline.

For each element, the absolute collected metal mass was modeled as a function of total collected particle mass and K_{slow} using multiple linear regression after $\log_{10}$ transformation. The model was fit separately for Pb and Cr across the seven fire-altered material experiments:

$$\log_{10}(M_{metal}) = \beta_0 + \beta_1 \log_{10}(M_{RP}) + \beta_2 \log_{10}(k_{slow}) + \varepsilon$$

where M_{metal} is the collected airborne Pb or Cr mass, M_{RP} is the collected resuspended particulates mass, K_{slow} is the $PM_{2.5}$ decay constant, β_0 is the model intercept, β_1 and β_2 are fitted regression coefficients describing the relationships between metal mass and each predictor, and ε is the residual error term representing variation not explained by the model. Predicted values from each model were compared with observed $\log_{10}$-transformed metal masses using predicted-versus-observed plots (Fig. S14).

Table S1. General characteristics of the burned source materials and their resuspensible particle content.

Sample	Description	Total collection time (min)[1]	Total resuspensible dust mass (mg)
Palisade A	Sample collected from the center of the collapsed, fire-damaged garage, adjacent to rusted structural beams and various burned metal components.	105	3.0 ± 0.6
Palisade B	Sample collected from the interior of the hood of a small vehicle, which contained numerous pieces of heavily rusted metal.	26.0	0.56 ± 0.06
Palisade C	Sample collected from the area in front of the burned vehicle, near the garage door and the front of the vehicle.	85.0	4.4 ± 0.3
Eaton A	Sample collected from the residual debris surrounding the burned electric vehicle.	120	4.3 ± 0.5
Eaton B	Residue around a burned Tesla car	105	0.93 ± 0.09
Eaton C	Burned and melted metal planter located at the front of the house.	669	10.2 ± 0.7
Eaton D	Composite sample collected and mixed from multiple areas across the property, including residue around a car (60%), car engine (8%), inside a front seat and trunk of a car (4%), dishwasher (20%), and burned debris from the kitchen, storage room (8%).	256	8.2 ± 1

[1]Collection time is the duration from the start of the resuspension experiment until the $PM_{2.5}$ concentration inside the Windbox decreased below 35 μg m^{-3}. The collection time correlates with the amount of airborne PM in each experiment.

Table S2. Total K concentration across fires

Fire	K ng m^{-3}
Park	1274 ± 17.6
Fresno June Lightning Complex	218.8 ± 73.0
Boise	283.3 ± 12.7
Wapiti	321.0 ± 64.8
Red	233.2 ± 23.7
Lake	1136 ± 192.5
Shelly	199.0 ± 15.03
Middle Fork Complex	348.6 ± 14.8
Coffee Pot[1]	394.5
Diamond Complex[1]	296.6
Eaton Fire	752.0 ± 116

[1]Duplicate samples were measured for these samples, so the standard errors are not shown

Table S3. Geological classification, layer scoring, and acreage used to calculate the Geology Composition Index.[1]

	Geologic Layers	Geology classification	Layer Scores	Layer Acres	Total Fire Acres	Geological Composition Score
Eaton Fire	Granite and granodiorite	Felsic to intermediate	2.5	6452	14021	1.69
	Alluvium and terrace deposits	Sedimentary	1	5211		
	Schists	Metamorphic non-mafic	1	2325		

[1] The GCI information for wildland fires is shown in Namayandeh et al.[3]

623 **Table S4.** Metal enrichment across different source materials and aerodynamic diameter fraction

Element	Size	Palisades A	Palisades B	Palisades C	Eaton A	Eaton B	Eaton C	Eaton D
	Ultrafine	0.21	1.2	53	0.26	0.65	3.9	0.070
	Fine	0.15	2.5	0.70	0.21	0.92	4.5	0.75
	Coarse	0.14	2.6	0.62	0.17	1.2	4.8	0.90
Pb	Total	0.15	2.3	4.3	0.20	1.1	4.5	0.55
	Ultrafine	31	25	2.0	12	150	4.3	0.43
	Fine	7.1	19	0.87	3.2	5.3	5.2	4.9
	Coarse	1.2	9.9	0.60	1.7	4.5	5.5	7.7
Cr	Total	4.7	17	0.80	4.4	8.2	5.2	4.1
	Ultrafine	2.4	2.5	1.5	2.9	1.4	4.9	0.00042
	Fine	2.0	5.5	2.9	3.0	1.7	7.0	0.0062
	Coarse	1.2	5.0	1.7	1.4	1.3	7.6	0.0075
Ti	Total	1.6	4.7	2.1	2.3	1.5	6.8	0.0045
	Ultrafine	0.077	0.31	0.13	1.1	0	3.3	0.31
	Fine	0.042	0.57	0.34	0.73	0.11	4.4	2.8
	Coarse	0.043	0.79	0.81	0.63	0.30	5.0	2.5
Cu	Total	0.044	0.60	0.59	0.76	0.23	4.4	1.8
	Ultrafine	0.48	0.89	0.70	0.49	0	2.5	0.35
	Fine	0.32	1.8	0.82	0.32	0.29	1.9	4.1
	Coarse	0.21	1.7	0.90	0.26	0.65	2.6	5.2
Mn	Total	0.27	1.6	0.86	0.33	0.51	2.3	3.1
	Ultrafine	0.48	0.54	0.17	1.8	0	2.1	0.0021
	Fine	0.35	1.2	0.17	1.1	0.19	2.4	0.026
	Coarse	0.21	1.1	0.32	1.0	0.66	3.3	0.044
Fe	Total	0.28	1.0	0.26	1.2	0.48	2.7	0.023
	Ultrafine	5.5	2.1	3.5	1.0	1.3	2.4	0.014
	Fine	3.4	3.7	0.94	0.34	2.7	2.6	0.17
	Coarse	0.74	3.0	0.75	0.40	2.7	3.3	0.21
Ni	Total	2.0	3.1	1.0	0.51	2.7	2.8	0.13
	Ultrafine	0.89	1.6	1.1	2.8	7.2	3.5	0.000049
	Fine	0.56	3.7	1.1	2.2	2.2	4.3	0.00059
	Coarse	0.45	3.4	1.0	1.4	2.7	4.6	0.00069
Zn	Total	0.51	3.2	1.1	2.0	2.6	4.3	0.00043

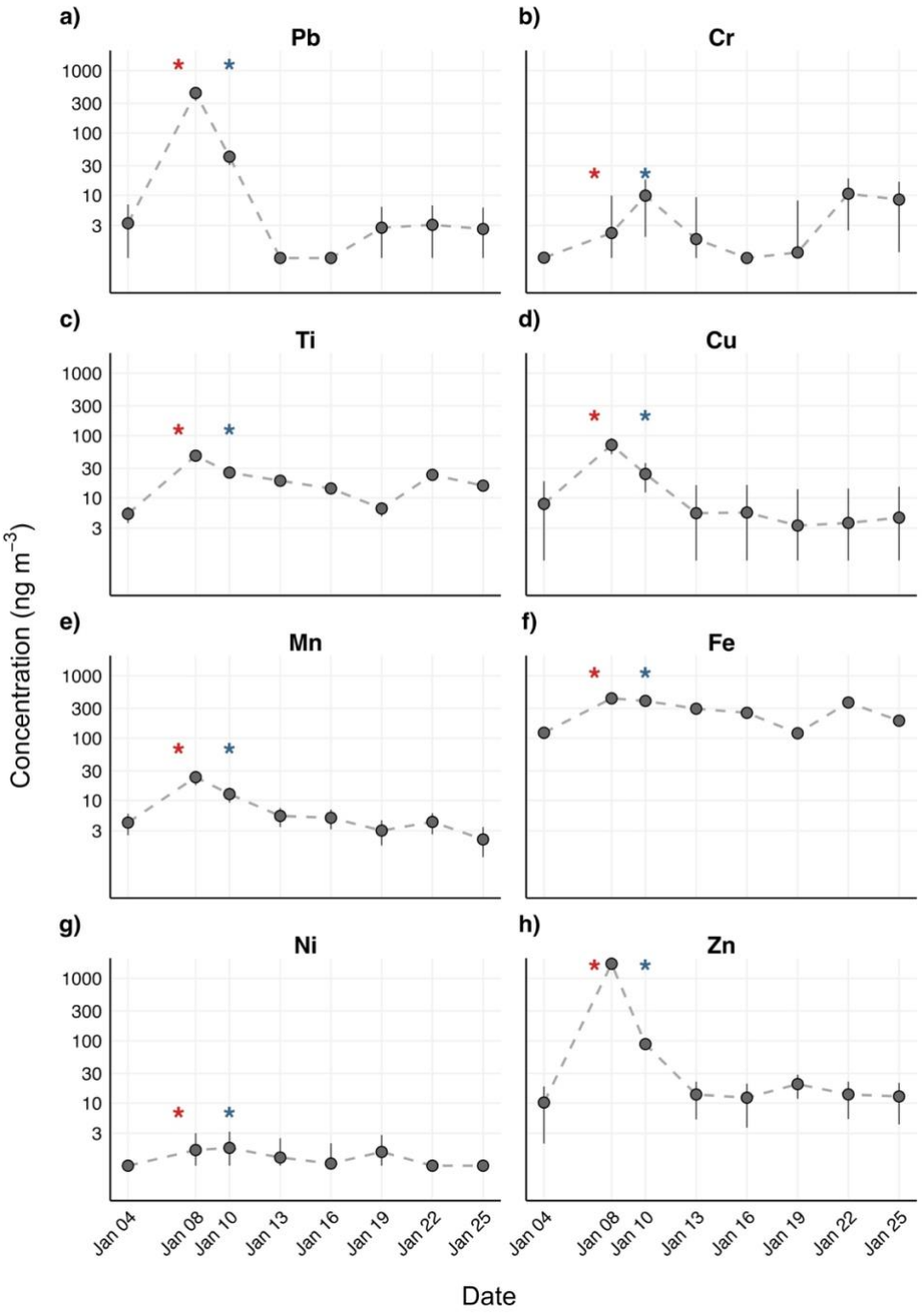

Figure S1. Temporal variation in metal concentrations in Eaton fire smoke. Red and blue asterisks indicate the fire start date and our smoke sample collection date, respectively. Error bars represent the reported uncertainty associated with each data point.

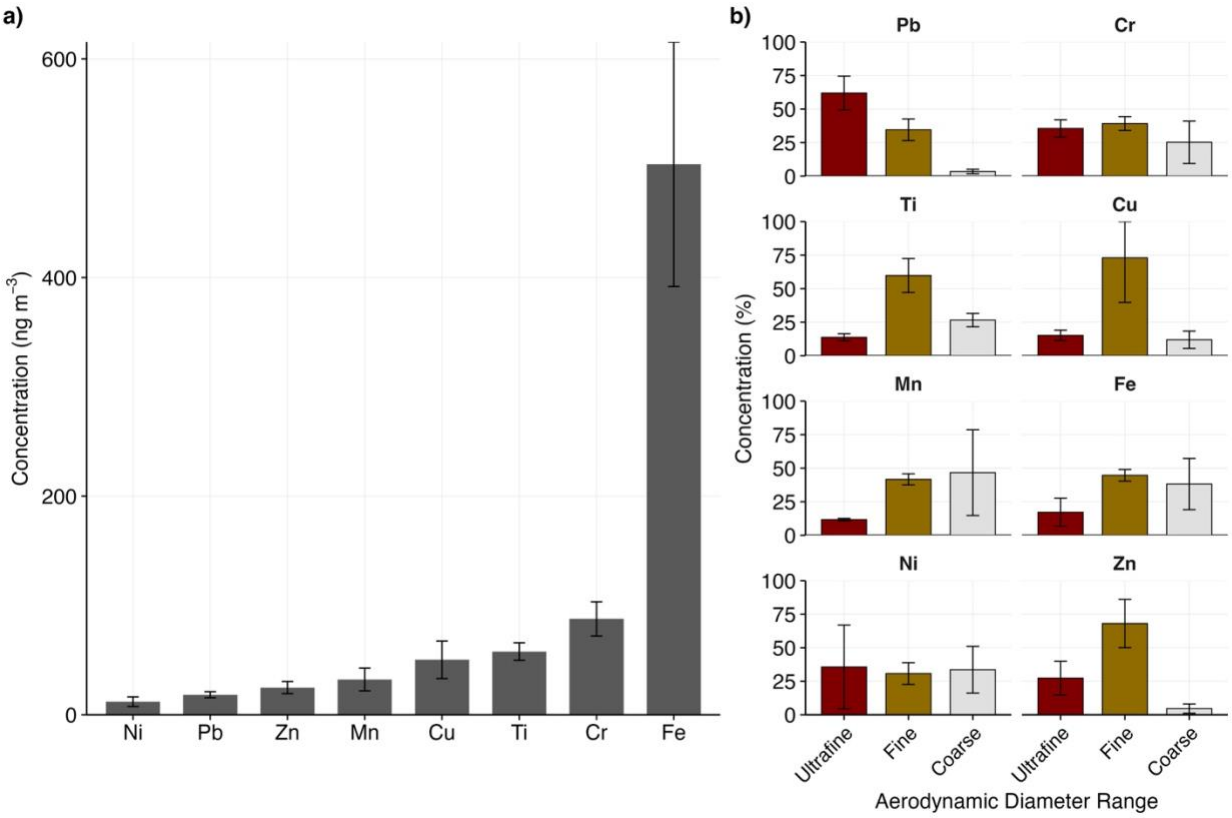

628

629 **Figure S2.** a) Total concentration (%) of metals in Eaton fire smoke (collected on Jan 10), b) Normalized

630 concentration of metals across particle-size fractions. Error bars represent standard errors (n=3)

631

632

633

634

635

636

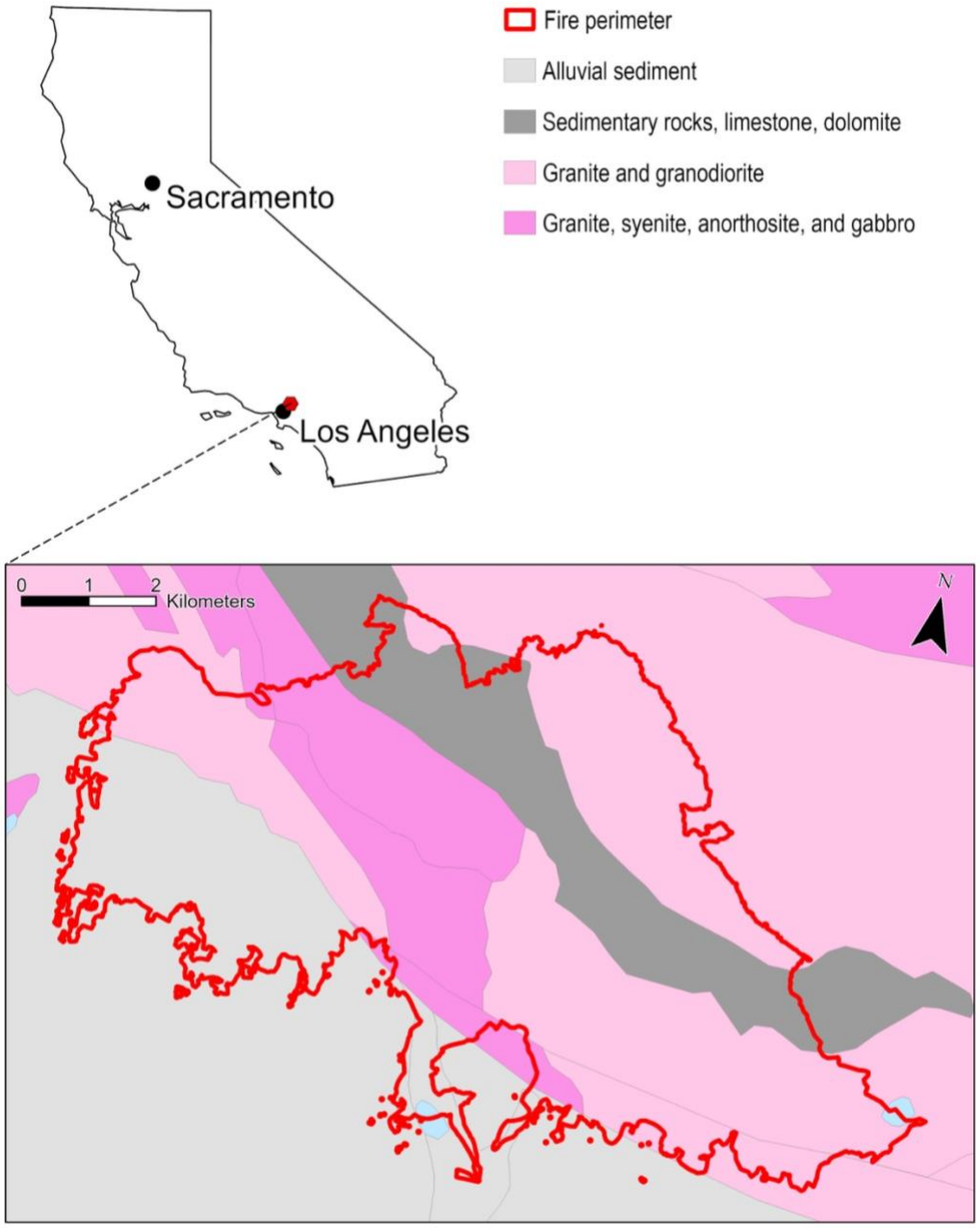

637

638 **Figure S3.** Geological map of the Eaton Fire perimeter.

639

640

641

Figure S4. Collection of burned source materials from fire-impacted structures and vehicles following the 2025 Los Angeles fires. EFD is not shown. General characteristics of the samples are provided in Table S1.

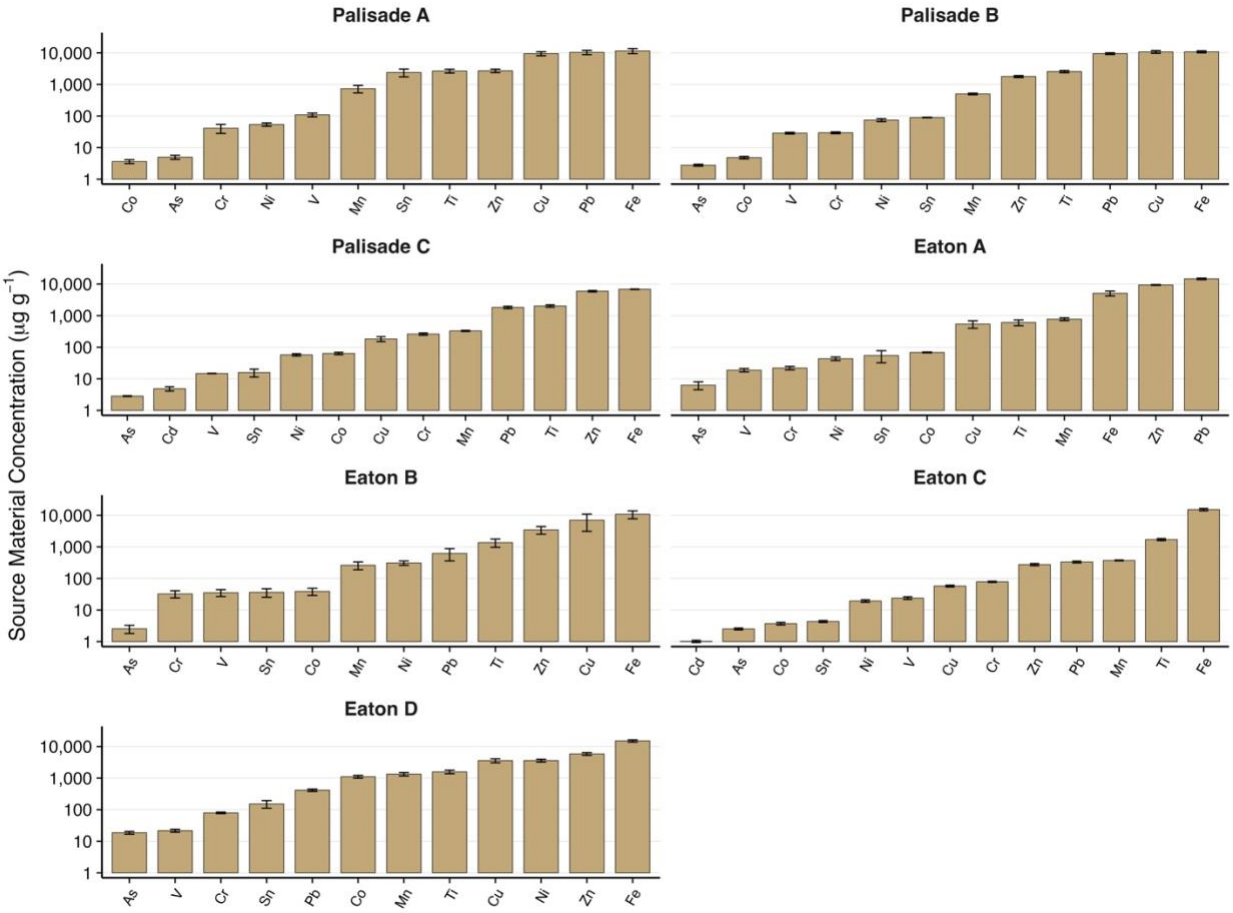

652

653 **Figure S5.** Metal concentrations in source materials collected from fire-impacted properties affected by the

654 Palisades Fire (Palisade A–C) and Eaton Fire (Eaton A–D). Error bars represent standard errors (n=3).

655

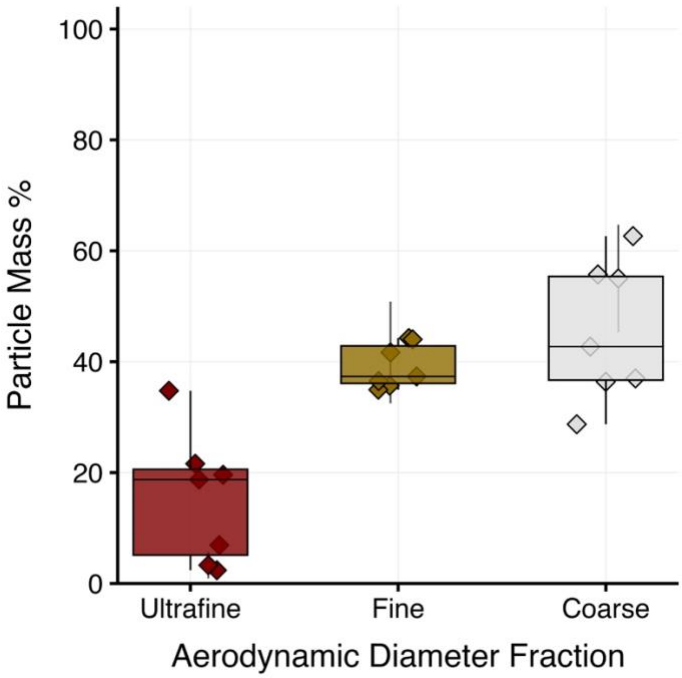

656

657 **Figure S6.** Percentage of airborne PM generated from the resuspension of source materials across different
658 size bins. Boxplots show airborne concentrations of ultrafine (<0.25 μm), fine (0.25–2.5 μm), and coarse
659 (>2.5 μm).

660

661

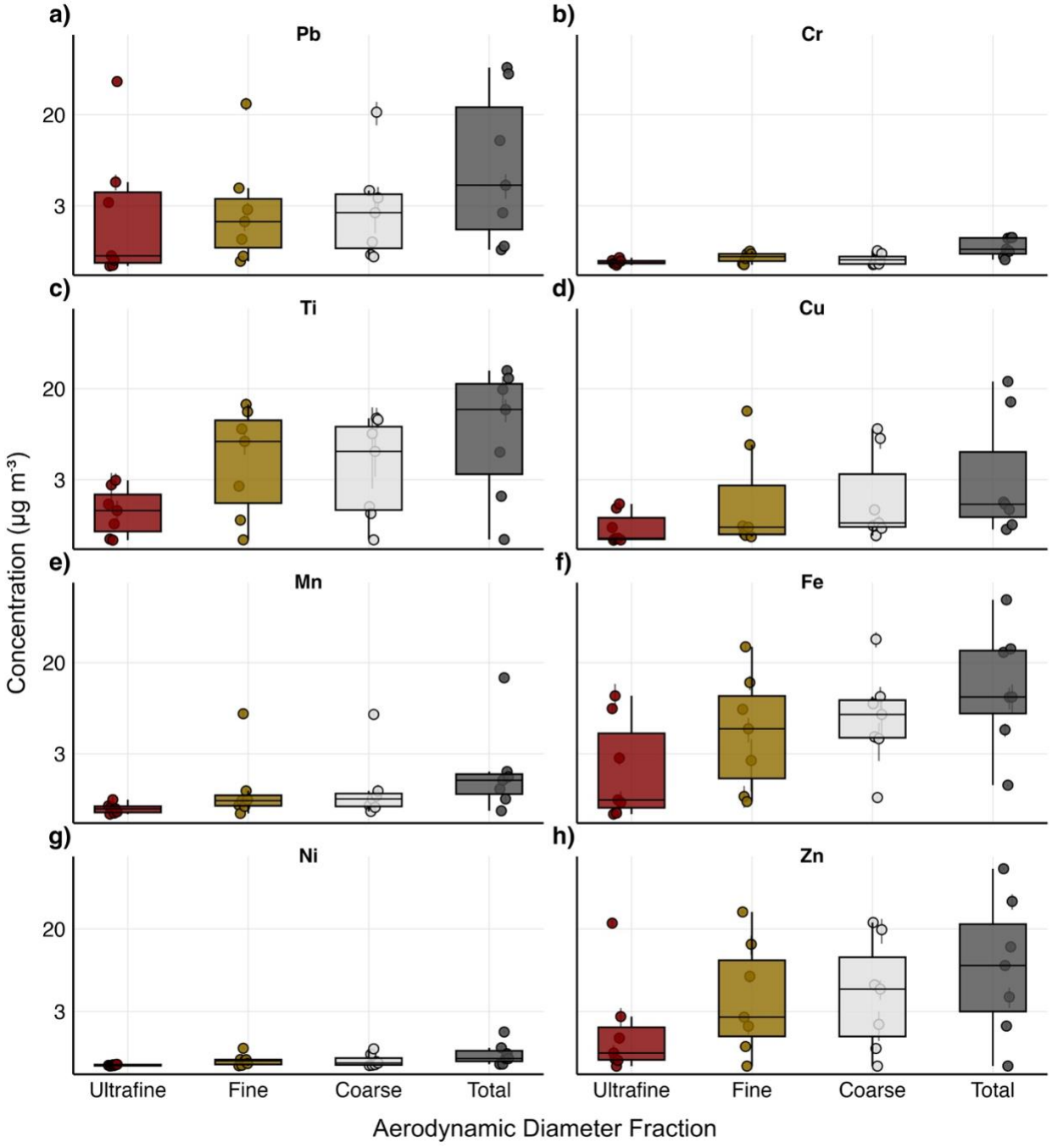

Figure S7. Concentrations of metals in air across aerodynamic diameter fractions generated from the resuspension of burned source materials.

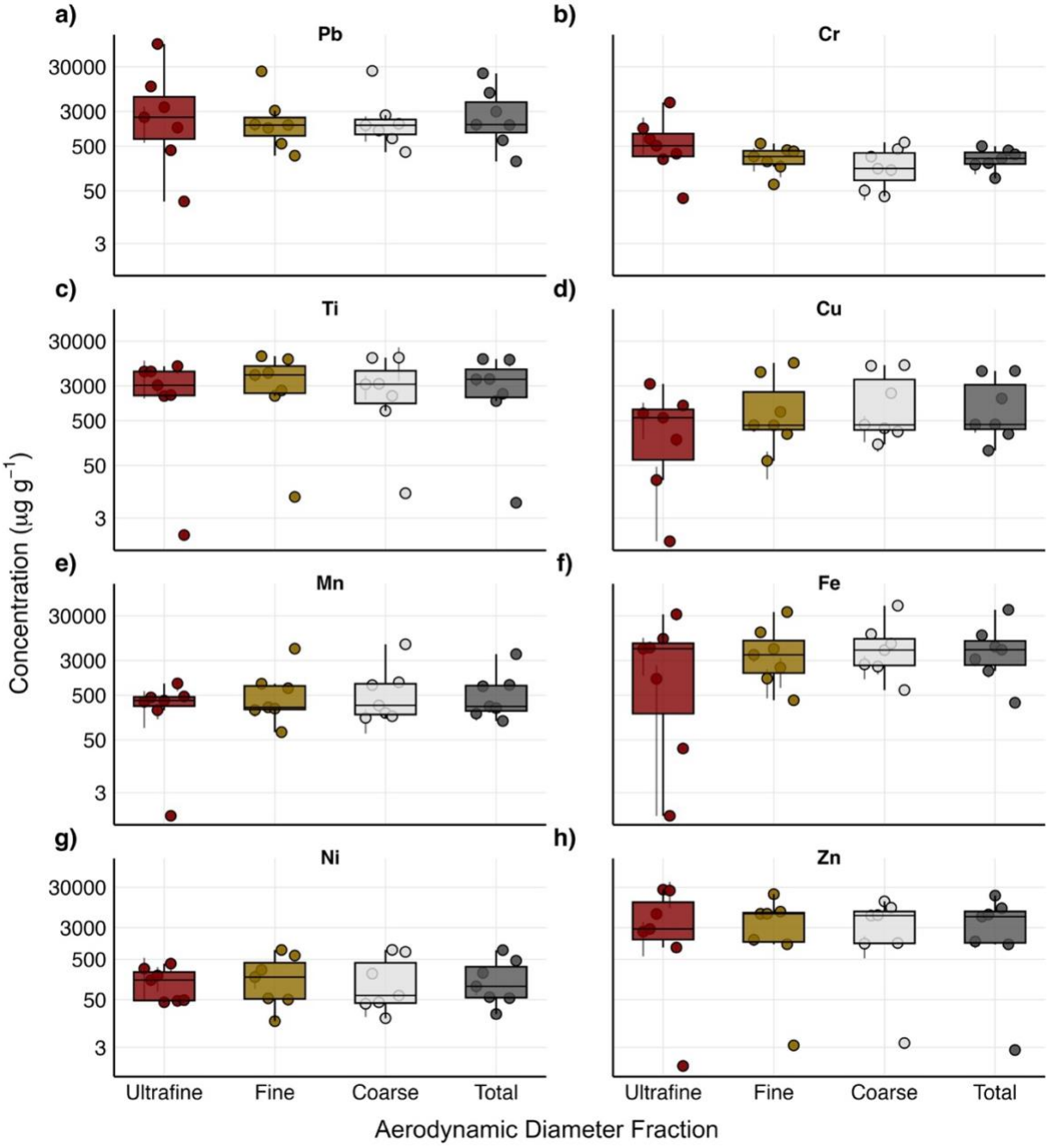

Figure S8. Mass-normalized concentrations of metals in resuspended particles generated from burned source materials across aerodynamic diameter fractions. Concentrations were calculated by dividing the mass of each metal collected on a size-resolved filter by the total mass of resuspended particles collected on the same filter.

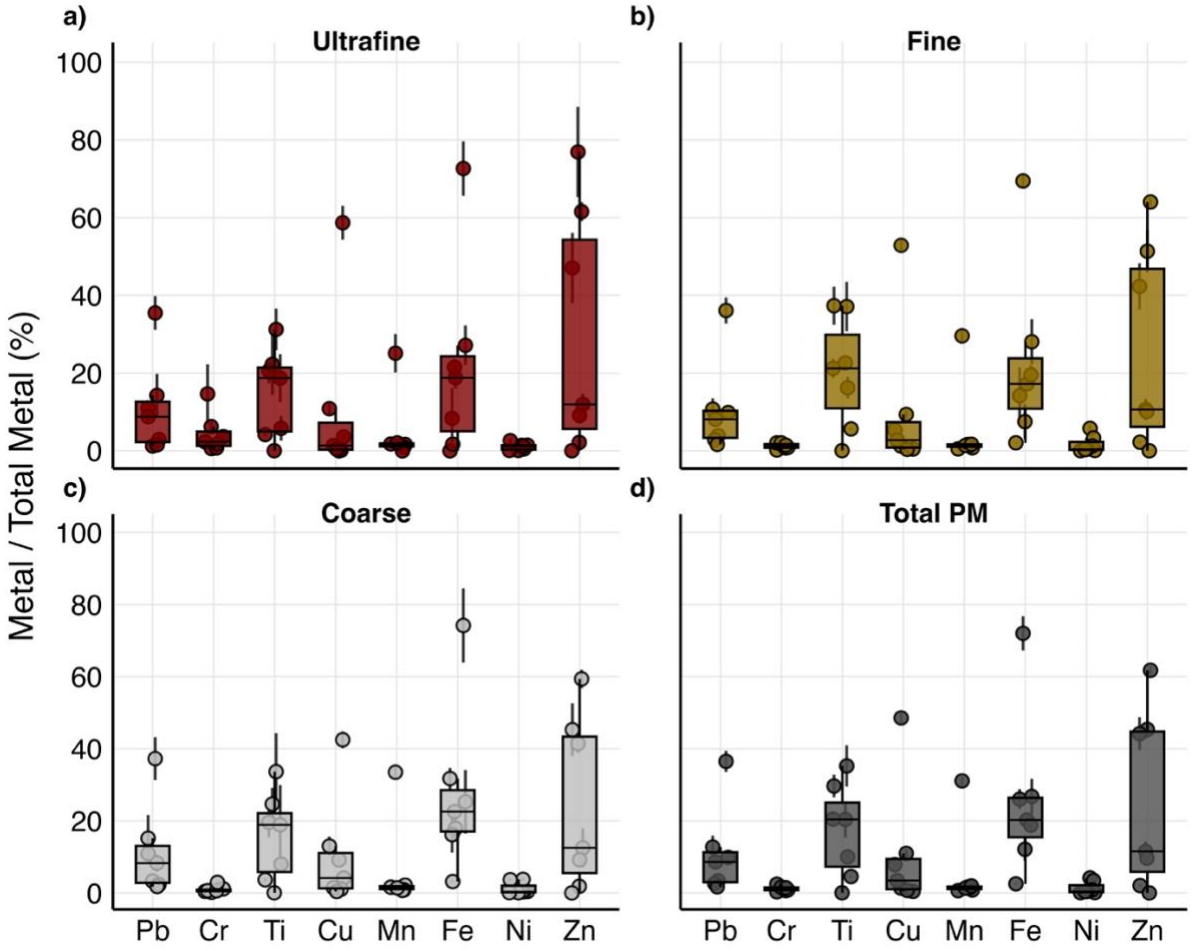

Figure S9. Relative contribution of each metal to the total measured metal mass in resuspended dust across aerodynamic diameter fractions. Percentages were calculated by dividing the mass of each metal by the total mass of all analyzed metals within the same aerodynamic diameter fraction.

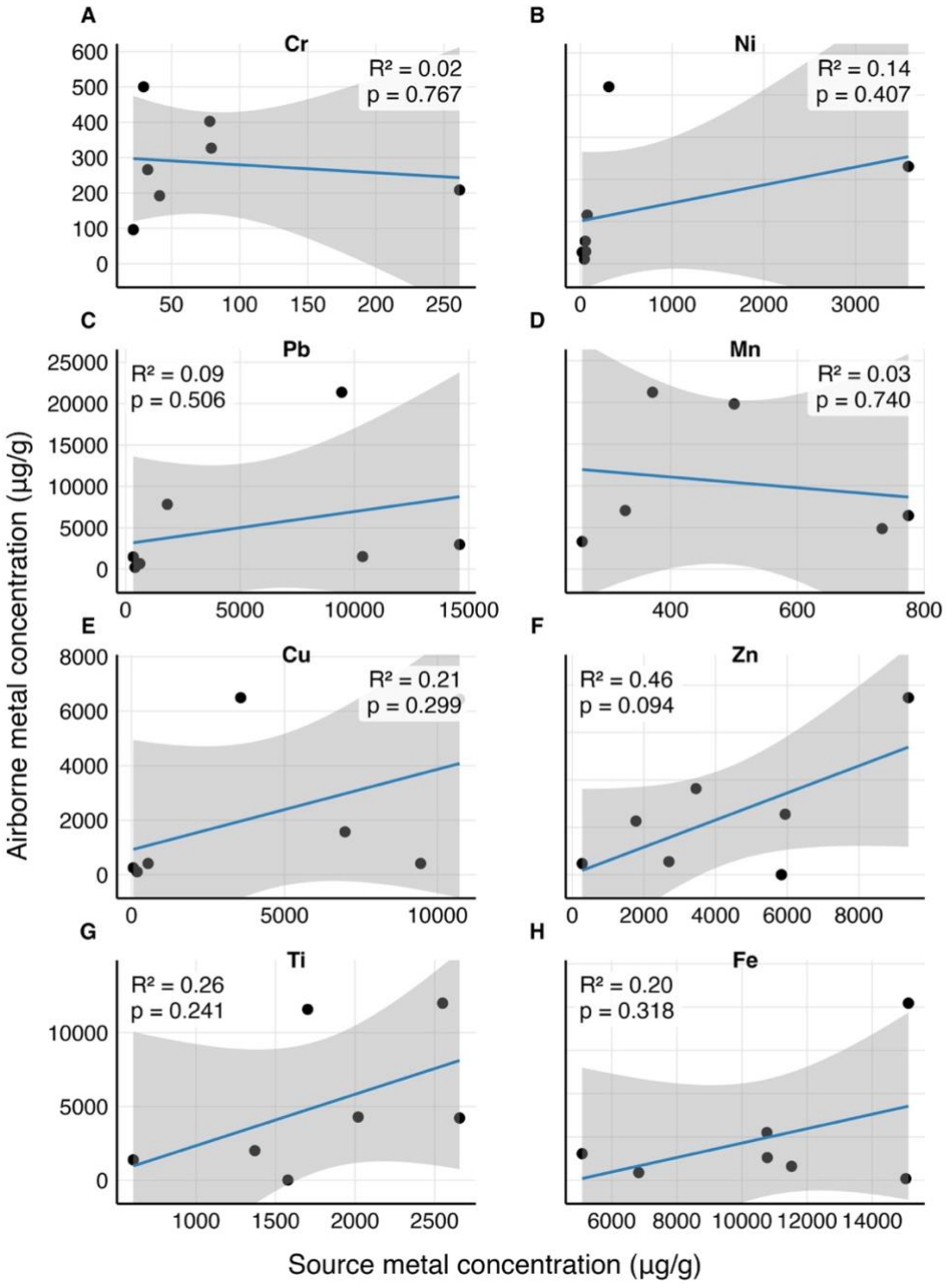

685

686 **Figure S10.** Relationships between metal concentrations in burned source materials and mass-normalized

687 metal concentrations in airborne resuspended dust.

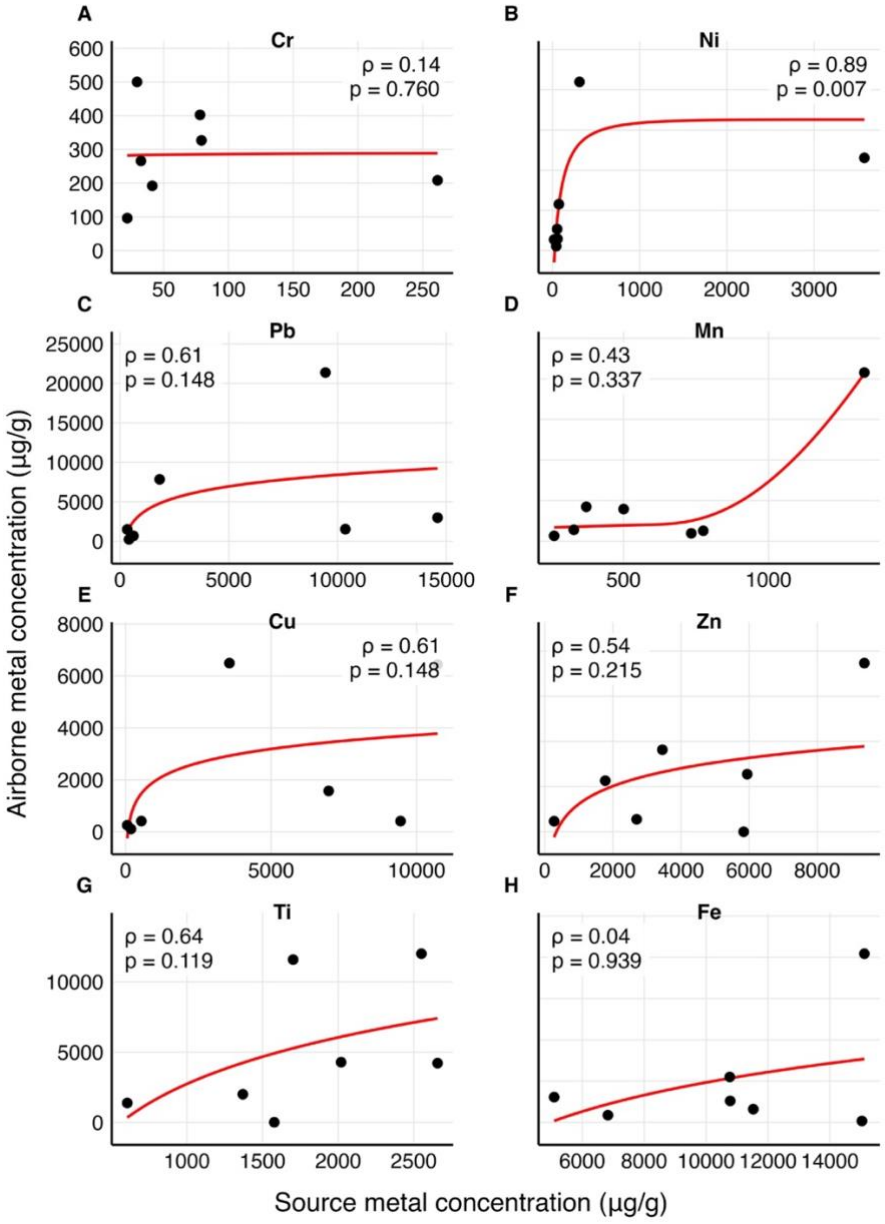

688

689 **Figure S11.** Non-parametric relationships between metal concentrations in burned source materials and

690 mass-normalized metal concentrations in airborne resuspended dust.

691

692

693

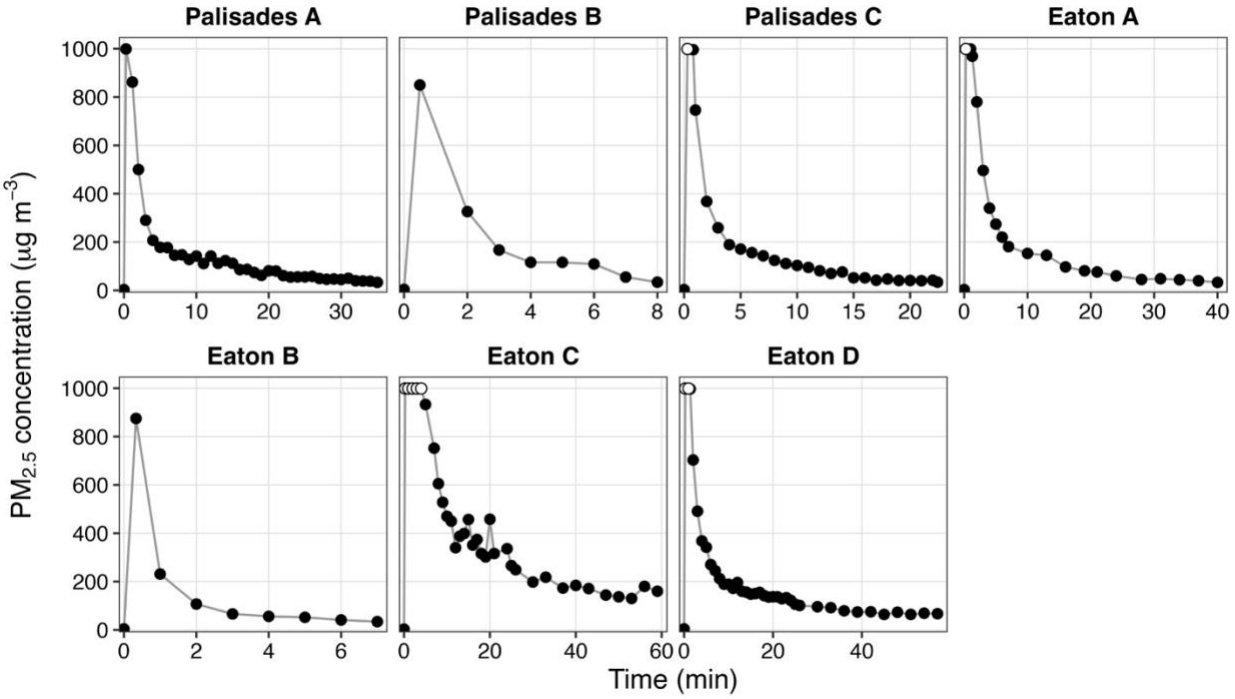

694

695 **Figure S12.** Temporal variation in $PM_{2.5}$ concentrations during windbox experiments. Open circles indicate

696 concentrations reported above the instrument measurement limit (>999 μg m^{-3}).

697

698

699

700

701

702

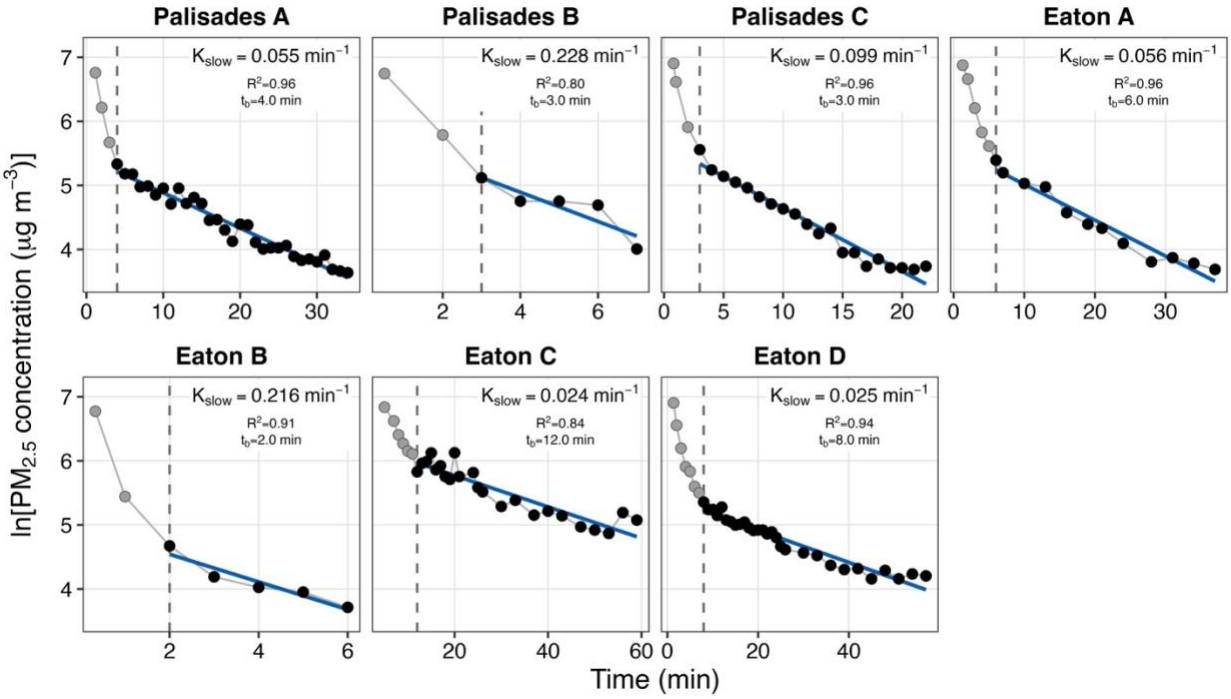

Figure S13. Estimation of the slow-phase $PM_{2.5}$ depletion rate during the experiments**.** The natural logarithm of $PM_{2.5}$ concentration is plotted against time for each fire-altered source material. Gray points represent the initial rapid-depletion phase, and black points represent the subsequent slow-depletion phase used to estimate K_{slow}. Dashed vertical lines indicate the selected transition time (t_b) between phases. Blue lines show linear fits to the slow phase, with K_{slow} calculated as the negative fitted slope.

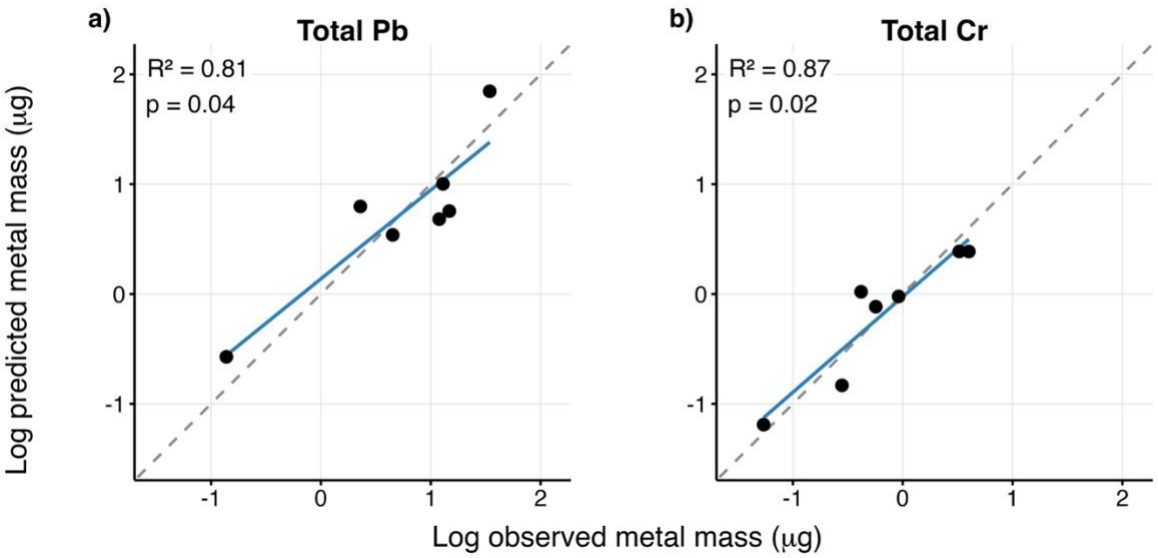

Figure S14. Predicted versus observed airborne mass for Pb and Cr. **Log**-transformed observed collected metal mass is compared with values predicted by the multivariate model incorporating total PM mass and the PM decay constant, k. The blue line is fitted regression line of predicted vs observed values. The dashed line represents the 1:1 relationship between observed and predicted values.

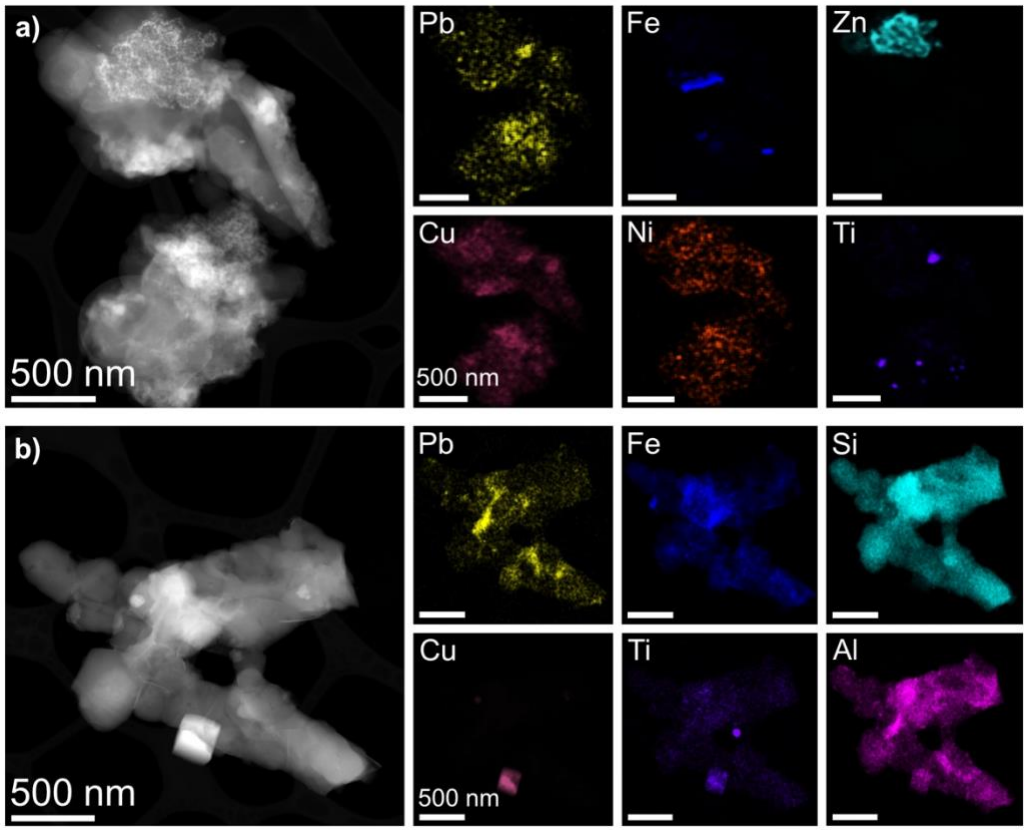

Figure S15. Scanning transmission electron microscopy (STEM) images and corresponding elemental maps. (a) Aggregates of multi-metal particles containing Pb, Cu, Fe, Ni, Zn, and Ti in smoke. Pb-rich nanoparticle aggregates are distributed throughout the particles and are closely associated with Cu. (b) Irregular Pb-bearing particle aggregate associated with Si, Al, Fe, Cu, and Ti in resuspensible dust from PFB. Elemental maps show that Pb is heterogeneously distributed within the particle, while Si and Al are broadly co-located across the aggregate, consistent with a mineral- or ash-derived particle.

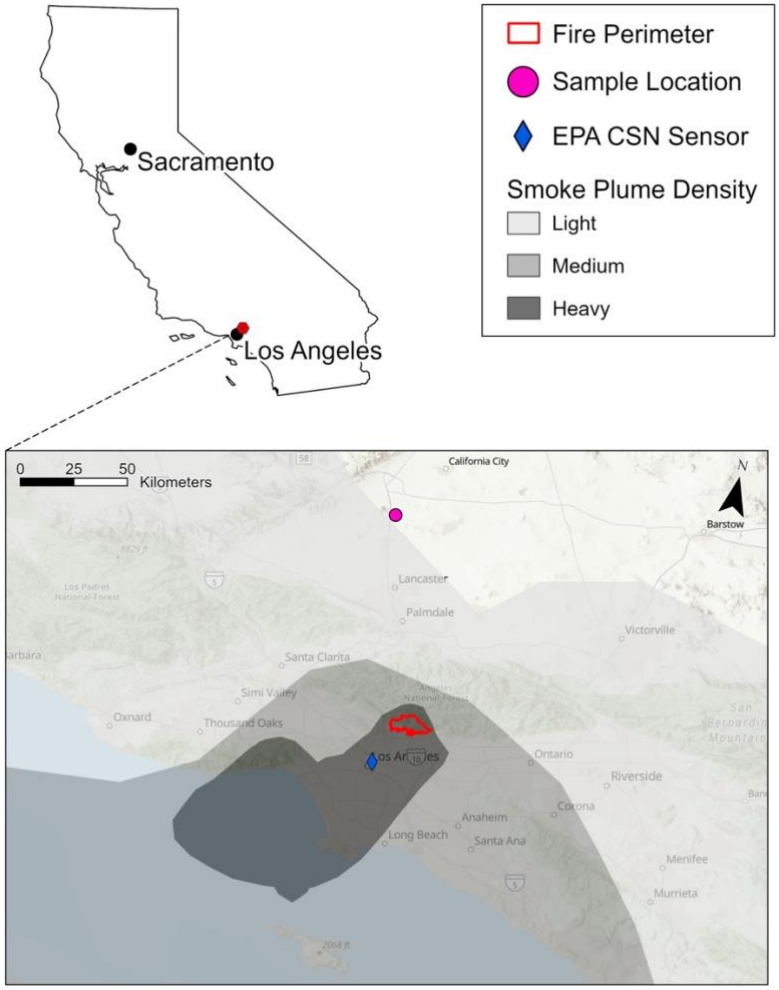

Figure S16. Smoke plume extent over sampling locations for Eaton Fire in southern California. Fire perimeters and smoke plume density are shown relative to sampling locations, demonstrating that samples were collected while the sites were within active smoke plumes. Locations of EPA CSN monitoring stations and sample locations are shown. The data reported by the EPA sensor are shown in Figure S1.

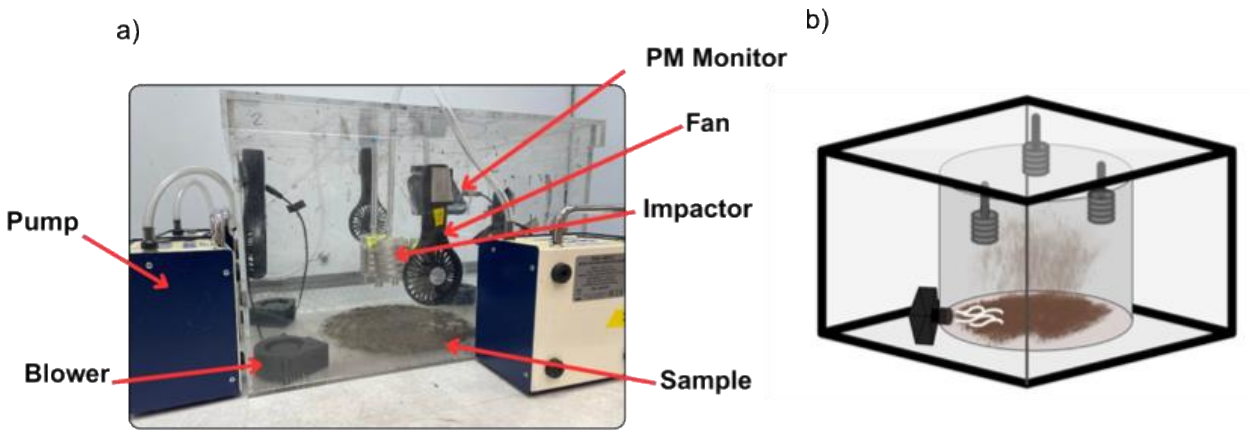

752
753
754 **Figure S17.** Windbox setup used to generate and collect resuspended dust from burned source materials.
755 (a) Photograph of the experimental system showing the enclosed chamber, internal fans/blowers, burned
756 source material placed at the center of the chamber, and active air samplers connected to cascade
757 impactors for size-resolved particle collection. (b) Schematic illustration of the windbox showing airflow-
758 driven resuspension of burned source material and collection of airborne particles.
759
760
761
762